European Journal of Cell Biology 103 (2024) 151383

Contents lists available at ScienceDirect

European Journal of Cell Biology

journal homepage: www.elsevier.com/locate/ejcb

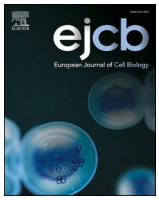

Helical motors and formins synergize to compact chiral filopodial bundles: A theoretical perspective

Ondrej Maxian [a,c,d], Alex Mogilner [a,b,*]

[a] Courant Institute, New York University, New York, NY 10012, USA
[b] Department of Biology, New York University, New York, NY 10012, USA
[c] Department of Molecular Genetics and Cell Biology, University of Chicago, Chicago, IL 60615, USA
[d] Institute for Biophysical Dynamics, University of Chicago, Chicago, IL 60615, USA

ARTICLE INFO

Keywords:
Actin bundle
Chirality
Filopodium
Filament buckling
Twisting
Formin

ABSTRACT

Chiral actin bundles have been shown to play an important role in cell dynamics, but our understanding of the molecular mechanisms which combine to generate chirality remains incomplete. To address this, we numerically simulate a crosslinked filopodial bundle under the actions of helical myosin motors and/or formins and examine the collective buckling and twisting of the actin bundle. We first show that a number of proposed mechanisms to buckle polymerizing actin bundles without motor activity fail under biologically-realistic parameters. We then demonstrate that a simplified model of myosin spinning action at the bundle base effectively "braids" the bundle, but cannot control compaction at the fiber tips. Finally, we show that formin-mediated polymerization and motor activity can act synergitically to compact filopodium bundles, as motor activity bends filaments into shapes that activate twist forces induced by formins. Stochastic fluctuations of actin polymerization rates and slower cross linking dynamics both increase buckling and decrease compaction. We discuss implications of our findings for mechanisms of cytoskeletal chirality.

1. Introduction

The cytoskeleton shapes cells, tissues and organs (Fletcher and Mullins, 2010). Actin filaments are crucial elements of the cytoskeleton, and are polar and chiral right-handed helices with distinct plus and minus ends (Jegou and Romet-Lemonne, 2020). Molecular polarity, helicity and chirality of actin filaments propagate to cytoskeletal arrays, cells, and tissues, which ultimately underlie important left-right asymmetries in development and complex organisms (Inaki et al., 2016). However, the mechanisms of this propagation remain largely unclear.

Two mechanical molecular processes were proposed to be the starting points for chirality generation in the cytoskeleton (Naganathan et al., 2016; Jegou and Romet-Lemonne, 2020). The first one is based on the action of formin, the "leaky capper" protein that stays on the growing plus end of the filament, thereby mediating the process of actin polymerization (Fig. 1A). Because of actin's helical structure, formin can rotate around the filament axis in the process of growth, or, if formin is fixed to a larger structure, an actin filament could rotate by being "extruded" from formin (Mizuno et al., 2011), in which case formin effectively applies a torque to the filament. The second symmetry-breaking process could be triggered by myosin molecular motors that in some cases move helically around actin filaments (Nishizaka et al., 1993), effectively applying both torque and force. Our goal here is to computationally examine how these two pathways of chirality emergence act in a small polar actin bundle.

There is no consensus yet on the chiral action of formins. On the one hand, Mizuno et al. observed actin filaments rotating clockwise (CW), if viewed from the plus end, when growing with a formin on the plus end (Mizuno et al., 2011). This would imply a formin-generated CW torque on the filament plus end. On the other hand, no supercoiling was observed when long actin filaments grew from formins attached to a substrate (Kovar and Pollard, 2004). If there is a formin-generated torque, then a sufficiently long filament must supercoil, so this result implies no or insignificantly weak torque. To explain this paradox, (Shemesh et al., 2005) proposed a mechanism where formins twist actin filaments until this twist is no longer energetically favorable, at which time a "screw" rotation dissipates the torsional strain. This model was expanded in the recent study (Li and Chen, 2022), which considered it in tandem with two other possible models of formin-actin interaction. The conclusion of that study is that, for some mechanisms, the formin can apply a rapidly fluctuating torque on the filament end, and that the net

* Correspondence to: Courant Institute, NYU, 251 Mercer St, New York, NY10012, USA.
E-mail address: mogilner@cims.nyu.edu (A. Mogilner).

https://doi.org/10.1016/j.ejcb.2023.151383
Received 24 July 2023; Received in revised form 19 December 2023; Accepted 30 December 2023
Available online 11 January 2024

Nomenclature

CW	(clockwise).
CCW	(counterclockwise).

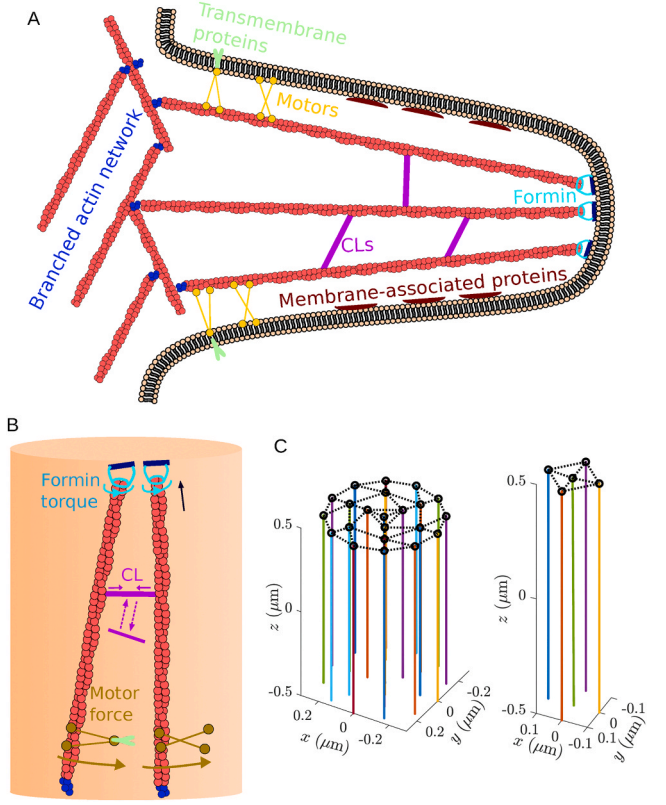

Fig. 1. Model filopodia. (A) Biological schematic. A filopodium is composed of long, almost parallel, cross-linked actin filaments emerging from a dense lamellipodial network at the base. In the model, the polymerization at the tip is driven by formins, which are attached to the membrane/protein tip complex. The filopodium is encased in a membrane, which is covered with a dense network of membrane-assocated and transmembrane proteins constituting an effective "sheath" around the actin bundle. Myosin motors associate with the sheath and interact with actin filaments. (B) Modeled mechanics of the bundle. We consider a system of fibers (slender inextensible rods), which are connected by crosslinks modeled as springs. The branched actin network at the base is reduced to a clamped condition, while the action of formin at the tips becomes a torque boundary condition (combined with polymerization at a variable rate). We model motors with their cargo domains attached to a firm cylindrical membrane/protein sheath and motor domains applying forces directed tangential to the cylindrical surface, with the main force component perpendicular to the bundle axis, and a minor force component downward along the axis. (C) Geometries of the two filopodial bundles that we use in this study. We consider a five-filament filopodium (right) and a 22-filament filopodium (left). The first is used to build intuition about the second, which has a realistic number of fibers. Initially, the fibers are connected at the tips by cross links.

torque would be on the order of 100 pN · nm (Li and Chen, 2022). Moreover, that model (Li and Chen, 2022) predicts that the torque can be both CW and counterclockwise (CCW).

Several reports pointed out that some myosin motors are helical, walking around actin filaments along a helical path, so when the motors are attached to a larger structure, they not only exert a force on a filament, but also apply torque to it. Tanaka et al. reported that muscle myosin could be either a CW or a CCW motor (Tanaka et al., 1992), while a later study proposed it to be exclusively CW motor (Nishizaka et al., 1993). (In the literature, the terms "right-" and "left-handed"' are often used for the helical motors; here, to avoid confusion, we call them CW and CCW (rotating the filament CW and CCW if viewed from plus end), respectively. Our view direction will always be from the plus end when mentioning CW or CCW rotation, and so we will skip mentioning the point of view henceforth.) Myosin V was reported to be a CCW spiral motor (Cheney et al., 1993; Ali et al., 2002a), while myosin X was shown to be a CCW helical motor that moves helically around actin bundles, rather than just single filaments (Sun et al., 2010). Myosin 1D was found to be a CCW motor (Lebreton et al., 2018). Twirling of actin by myosins II and V was observed in a gliding assay (Beausang et al., 2008).

These formin and myosin actions are relevant for actin bundle dynamics in filopodia, which are finger-like bundles which protrude from the cell edge and measure several to tens of microns in length and tenths of microns in diameter (Jacquemet et al., 2015). They consist of a parallel bundle of 10 to 30 actin filaments (Jacquemet et al., 2015) crosslinked by fascin (Aratyn et al., 2007) and other crosslinkers. The filaments polymerize and grow at the plus ends at the filopodial tip (Mallavarapu and Mitchison, 1999), while the bundle undergoes retrograde flow (away from the tip) driven by myosins at the filopodial base (Forscher and Smith, 1988; Aratyn et al., 2007). Filopodia play a variety of mechanical and sensory functions (Davenport et al., 1993) and are implicated in wound healing (Wood et al., 2002), cancerogenesis (Arjonen et al., 2011) and development (Fierro-González et al., 2013). Here, we consider slow-growing filopodia, in which electron microscopy shows actin filaments that are continuous all the way from the lamellipodium to the filopodial tip (Svitkina et al., 2003; Li et al., 2023).

Several examples of chiral filopodial behavior have been reported. For example, it was shown that actin filaments in filopodia flow toward the cell body, rotating in the CCW direction (Forscher and Smith, 1988). Individual filopodia were observed to rotate around their longitudinal axes in the CCW direction (Tamada et al., 2010), in a myosin-V-dependent way. Adherent filopodia, formed during the spreading of cells, tended to change the direction of their extension in a chiral fashion, acquiring a left-bent shape, if viewed from above, in a myosin X- and formin-dependent way (Li et al., 2023). Most notably, not only chiral movements, but also buckling and CCW helical rotation, as well as twisting and coiling of the filopodial actin bundle were reported (Leijnse et al., 2022). These deformations were myosin-, but not formin-dependent (Leijnse et al., 2022).

In filopodia, formins are at the tip, capping and elongating filaments' plus ends (Mellor, 2010; Alieva et al., 2019). Formins there are a part of the "tip complex," a dense large protein patch that may or may not be relatively rigid (Mellor, 2010). Some formin species attach to the membrane or cortex by a specialized domain, which in turn is elastically connected to the actin-elongating formin domains (Chesarone et al., 2010). Thus, there is a possibility that formins are mechanically restrained and apply a net torque to the growing filament ends. In our model, we will examine the possible CCW formin-generated net torque (Fig. 1A,B), and then also consider changes in model predictions when the torque is CW.

Various types of myosin motors are found at different parts of filopodia (Leijnse et al., 2022). For example, there is abundant expression of myosin V at the base of filopodia (Evans et al., 1997). There, myosin V can be connected to organelles or microtubules (Tamada et al., 2010). Myosin II is also located at the base of filopodia (Alieva et al., 2019), where it pulls on the bundled filaments (Sheetz et al., 1992; Medeiros et al., 2006; Nemethova et al., 2008). At filopodium initiation, myosin X molecules are recruited to the membrane near the base (Watanabe et al., 2010). Later, myosin X (Zhang et al., 2004), as well as integrins (Hu et al., 2014) become associated with the membrane and the sub-membranous protein coat surrounding the actin bundle (Fig. 1A). Leijnse et al. proposed that myosin X associates with integrins and that myosin V associates with cargo that is part of the sub-membranous

protein coat (Leijnse et al., 2015a), and that there are effective forces between the bundle filaments and integrin- and BAR-connected motors on the filopodial sheath. It is thus reasonable to assume that helical myosin motors there are associated with relatively rigid structures of the filopodial sheath, and that these motors' powerstrokes are applied to the outer filaments of the bundle, oriented diagonally relative to the filament centerlines, with components along the circumference of the filopodial bundle that rotate, or spin, the filaments around the filopodial axis. In the model, we will consider only CCW myosin-generated net torque (Fig. 1A,B), since we need only consider the direction of the myosin torque *relative* to that of formin (for which we consider both directions).

Filopodial actin bundles are wrapped with membrane, which affects the bundle mechanics (Pronk et al., 2008; Daniels and Turner, 2013). However, the inside of the filopodial membrane "sheath" is densely coated with a finely structured polymeric scaffold (Mattila and Lappalainen, 2008; Zhao et al., 2011; Linkner et al., 2014) that includes BAR domains, dynamin and cortactin copolymerized into ring-shaped complexes twined around the actin bundles (Yamada et al., 2013). These and other membrane-associated proteins can significantly modulate the shape and mechanics of the membrane (Mattila and Lappalainen, 2008).

The general questions we wish to answer in this study are: how do the chiral molecular mechanics of individual filament/myosin/formin actors play out on the scale of cytoskeletal arrays, creating collective chirality of actin filaments? Would not crosslinking interfere with collective chirality (one would imagine that stapling two filaments together prevents their rotation)? And, do myosins and formins cooperate or inhibit each other's actions? To address these questions, we numerically simulate a crosslinked filopodial bundle under chiral myosin and/or formin actions and quantitatively examine the collective buckling and coiling response. We find that the myosin spinning action effectively "braids" the actin bundle, compacting it, generating buckling, and enhancing the crosslinking. Stochastic fluctuations of actin polymerization rates also contribute to filament buckling and bending of the bundle. Faster turnover of transient crosslinks removes the constraints that give buckling, thereby attenuating it, but at the same time enhances coiling and compaction of the bundle. Formin-generated twisting is much less effective than myosin-generated spinning in inducing filopodial coiling; however, with myosin activity, co-rotating formins are essential to give proper bundle compaction.

2. Materials and methods: computational model

In a recent combined experimental-theoretical study, the emergence of chirality and twist in filopodia was modeled by considering the actin bundle as a continuum active polar gel (Leijnse et al., 2022). In our case, the relatively small number of filaments and associated molecules in filopodia makes a discrete approach, in which filaments are treated as elastic rods under the action of motor forces, more appropriate. Successful mathematical analyses of deformations of bent and twisted rods (Stump, 2000) and buckling of actin filaments (Berro et al., 2007) and bundles (Martiel et al., 2020) allow us to build a detailed mechanical model of a dynamic filopodial bundle. Here, for the sake of biologist readers, we explain the computational model, schematic of which is shown in Fig. 1A,B mostly in words; the details are described in the Supplemental Material (SM).

Actin filament mechanics: We adopt our published model (Maxian et al., 2022) to describe actin filaments as cylindrical, slender, inextensible elastic rods undergoing and resisting bending and twisting deformations. The filaments, which we sometimes call fibers, move, rotate and deform under the influence of the following forces and torques:

- Elastic bending force tends to straighten the filament's centerline.
- Elastic twisting force tends to minimize the filament's twist (relative rotation of neighboring cross sections around the centerline).
- Viscous resistance from the movement of the filament through the fluid it is immersed in.
- Elastic force between neighboring filaments generated by deformations of the crosslinks that couple pairs of filaments.
- Steric force between pairs of filaments that are in touch with each other, preventing one filament from passing through another.
- Active force generated by myosin motors, which we will call motor force for brevity.
- Active torques generated by formins.

Boundary conditions: The filaments at the base, $z = 0$, are cantilevered into the actin cortex of the cell and clamped, so their positions and orientations, as well as the orientations of the filament cross sections at the base, do not change in time. This formulation does not contradict the possibility of the retrograde flow of actin, because the growth of actin network at the lamellipodia leading edge effectively keeps the filopodial base at $z = 0$. The plus ends are free to move and twist.

Motor forces: As shown in Fig. 1A,B and discussed in the Introduction, we assume that helical motors are attached to the effectively rigid surface of the filopodial sub-membrane sheath and generate power strokes along a helical path on the cylindrical surface of a filament. The motors do not have to be immobilized to the sheath; if their cargo domains drift along the membrane with friction, this will also result in the effective helical force applied to the outer filaments of the bundle. The helical force has two components, one of which tries to move the filament retrogradely toward the filopodial base. We typically assume that this force component is significantly dampened because of the retrograde flow of the filopodial bundle (Evans et al., 1997). We discuss this in more detail in Section 3.3.2. The dominant force component is consequently directed along the circumference of the filopodium, so that this force spins the filaments around the long axis of the filopodium (in a circular trajectory). At a point $\boldsymbol{x}$, the force $\boldsymbol{f}^{(\mathrm{mot})}$ can be computed by first converting $\boldsymbol{x}$ into cylindrical coordinates (R, θ, z), and using these to define a vector tangent to the circle at $\boldsymbol{x}$, via $\boldsymbol{t} = (-\sin\theta, \cos\theta, 0)$. The force density is then given by $\boldsymbol{f}^{(\mathrm{mot})} = f_0^{(\mathrm{mot})}\boldsymbol{t}$ if $R \geq 3R_f/4$ and $z \leq c_m L$ (L is the filament length), so that the motors act only on the outer 1/4 and bottom c_m of the filopodium. Two parameters here defining the motor forces include $f_0^{(\mathrm{mot})}$, which is the magnitude of the force density in units of pN/μm, and c_m, the fraction of the filaments on which the motors act. As mentioned in the Introduction, we consider motors which spin filaments in a CCW direction around the filopodium.

Motor and formin torque: Depending on the location where motors apply force, the filament centerlines can experience torque. In most of our simulations, we will assume the motors apply force on the centerline, so that no torque is generated. Where noted, we will instead assume motor activity at the filament boundaries, which implies that motors exert a torque on the filament centerlines in the CCW direction (same direction as the motor forces) of magnitude $f_{\mathrm{mot}}^{(0)}a$, where a is the radius of the filaments. In Section 3.3.3, we compare simulations without motor torque to those that include it to determine its effect.

As discussed in the Introduction, it is sensible to model the action of formin via a fixed torque at the free end (where formin is bound). On the static ends, we use a no-rotation boundary condition, since we assume the filaments are clamped to the branched actin network there. In the absence of motor torque, the SM shows that the result of these boundary conditions is a constant angle of twist per unit length along the filament centerline. We reject as unphysical a boundary condition of a fixed angular velocity on the free end, and first consider a torque which tries to twist the filament in a CCW direction around the centerline, in the same direction as the motor spin. We also consider the effect of the opposite torque direction.

Crosslinking: In the model, the crosslinks connecting filament pairs are linear springs with finite rest length whose ends connect to the 1D centerlines of filaments by completely flexible joints. The crosslinking kinetics consist of unbinding with a constant, force-independent, rate,

and of possible crosslink binding to any pair of distinct filaments separated by a distance roughly equal to the crosslink rest length. When a crosslink unbinds, both of its ends dissociate from the filaments at once.

Steric forces: When any two points on distinct filaments become too close, we apply a strong, short-range repulsive force that prevents them from passing through each other, while not perturbing any dynamics of the non-overlapping filaments.

Modeling actin polymerization: Actin polymerization is modeled with elongation of a filament at its plus end with a certain rate $\dot{L}$. It was argued that in filopodia the polymerization is stochastic due to the relatively small size of the system and consequent large fluctuations of the actin monomer concentration (Lan and Papoian, 2008). One additional source of stochasticity could be persistently different chemical conditions of different filament plus ends, i.e. one filament's end associated with formin, another one with VASP protein, etc. To account for that, we first simulated growth rates constant in time but varying between the filaments. Then, we make the growth rate of each filament a random variable:

$$d\dot{L} = K_P(\dot{L}_0 - \dot{L})dt + \sigma\, dW, \tag{1}$$

where the constant $K_P = 2/\text{s}$ is chosen so that deterministic fluctuations relax to the base value $\dot{L}_0 = 0.5\ \mu\text{m/s}$ on timescales 0.5 s. The noise strength $\sigma = 0.05\sqrt{2K_P}$ is chosen so the (stationary) standard deviation of the growth rate is 0.05 μm/s. In simple words, the average rate is the same for all filaments, but each filament's rate independently fluctuates in time with certain variance. In the model, we neglect the experimentally-observed dependence of the polymerization rate on force and torque (Yu et al., 2017.

Model parameters: The elastic and mechanical parameters characterizing actin filaments, crosslinkers, motor and formin forces and torques, polymerization rates, crosslinker kinetics and viscous drag coefficients have all been measured or estimated in experimental literature. The full list of parameters, their values and respective citations are gathered in the Supplemental Table. We vary some of the parameters, such as formin torque, crosslinker kinetics and variance of the polymerization rates, to evaluate their effect on the bundle dynamics. The model predictions are relatively robust to few-fold changes in other parameters.

Quantification of the filopodial bundle's shape: In order to compare predicted filopodial dynamics and mechanics at different model regimes and parameters, we need to quantify the buckling and twisting of the filaments. Intuitively, we are interested in three parameters: the vertical extension of the filaments (in the direction of the bundle axis, or z direction), the filaments' bend, and their twist around the bundle axis. To quantify these, we transform the coordinates of each fiber from Cartesian to cylindrical, where the origin for the polar grid is set by the closest point on the central fiber. This gives a set of coordinates $(R(s), \theta(s), z(s))$ for each fiber. The vertical extension can then be tracked by looking at $z(L, t)$. The amount of twist can be quantified by the number of rotations around the axis of either the filament endpoints, $(\theta(L, t) - \theta(L, 0))/2\pi$, or their midpoints, $(\theta(L/2, t) - \theta(L/2, 0))/2\pi$. To study the amount of bend, we compute the curvature of the fibers (magnitude of the derivative of the tangent vector with respect to arclength) and average the curvature over the whole fiber (in the L^2 norm). We then normalize the curvature by the curvature of a circle of radius equal to the initial fiber length $L(0)$, which is $2\pi/L(0)$. Together, these statistics convey how bent and twisted the filaments are, and are similar to the quantifiers used in (Grason and Bruinsma, 2007; Tee et al., 2023) to measure chirality and twist. It is also useful to plot the traces or trajectories of the fiber endpoints over time projected onto the (x, y) plane.

Numerical procedure for simulating the actin bundle: At each computational step, current geometries of all fibers and engaged crosslinks are used to compute the elastic bending and twisting forces, steric and cross-linking forces, and motor and formin torques. By balancing the net forces and torques with viscous resistive forces, the linear and angular velocities of the filaments are calculated, and their geometries are updated. In addition, the increase of the filaments' lengths by polymerization is calculated, and some of the existing crosslinks are dissociated, while new crosslinks are engaged with filament pairs according to their dynamics. Marching in small time increments from step to step evolves the bundle. Here we use a time in seconds, which is a natural time scale for the cell-scale forces and viscosities. As discussed in the SM, twist equilibrates $\mathcal{O}(1/\epsilon^2)$ faster than bending (Powers, 2010), where ϵ is the fiber aspect ratio. As such, in our simulations twist deformations, while technically dynamic, are typically in a steady state controlled by the amount of the formin twist (see the SM).

3. Results

Our results section is laid out as follows: in Section 3.1, we consider simulations with formin-mediated polymerization and torque, but without motors, demonstrating that there is no collective buckling or coiling in this case. We introduce motors without polymerization in Section 3.2, demonstrating that filaments in motor-induced coils tend to splay out. We combine the two mechanisms in Section 3.3, where we demonstrate that the motor-induced bending of fibers combines with formin-induced twist to compact bundles.

3.1. Polymerizing bundles without motors are typically straight

We first consider simulations of five-filament bundles, in which there is a central filament and four parallel peripheral filaments, the minus ends of which are located on the vertices of a square (right panel of Fig. 1C), with polymerization and no motor activity. We consider two potential mechanisms by which filopodia could take on bent shapes: filament supercoiling (Bibeau et al., 2023) and unequal polymerization rates.

3.1.1. Actin supercoiling above a critical twist density

Linear stability analysis of the model equations (see the SM) states that the critical twist, above which an actin filament supercoils, corresponds to 2.4 360-degree turns of the plus end. We test this prediction numerically by applying 2 turns to the plus end and observing that the filament relaxes to a straight shape, and then applying 3 turns to the plus end and observing that the filament supercoils (Fig. S1).

Figure S1 shows the complete phase diagram of supercoiling behavior as a function of twist density and filament length, which comes from (S26) in the SM. The results of (Bibeau et al., 2023), who for small applied forces found a supercoiling threshold at roughly 0.2 rotations per micron with filaments of length 7–20 μm, validate our physical model. According to our estimates, the characteristic formin-generated torque $N_L = 0.1\ \text{pN}\cdot\mu\text{m}$ will result in ≈ 0.4 turns per μm, so formin will not generate supercoiling unless filaments become 6 μm long (red circle in Fig. S1), which we will not consider here.

3.1.2. Buckling generated by polymerization, alleviated by transient crosslinking

Another way to get a nontrivial shape of the filopodium is polymerization with unequal or varying rates. To illustrate this, we first consider an extreme case in which the central filament is the only one that grows in time. In Fig. S2, we simulate the five-filament bundle with the plus ends permanently crosslinked (imitating the filopodial tip complex), allowing the central filament to polymerize at rate 1 μm/s until it reaches length $L = 2$ μm. Initially, the central filament grows linearly, stretching the crosslinks. When the crosslinking force becomes too strong, the central filament buckles (at $t = 0.2$ s). The buckled filament then drags other filaments with it, which buckles the bundle as a whole.

Interestingly, supercoiling of filaments attenuates this effect. We illustrate this in Fig. S3, where we apply a larger amount of twist on the

central filament. The increased twist gives supercoiling of the *central* filament, which can then grow in length by increasing the length of coiling in the interior of the bundle, rather than buckling and pushing the peripheral filaments.

In Fig. 2, we extend the unequal polymerization concept to the more biologically-realistic scenario of filaments with varying polymerization rates centered around a constant mean. First, we consider the five-filament bundle with permanent crosslinks at the filament plus ends. Each filament has a prescribed random growth rate which is drawn at $t = 0$ from a normal distribution with mean 0.5 μm/s and varying standard deviation (0.2, 0.1, or 0.05 μm/s), and then does not change in time. To prevent fibers from getting too long, we stop fibers from lengthening when the length gets longer than double the initial length of 1 μm. One simulation with growth rate standard deviation 0.1 μm/s is shown in Fig. 2A.

In Fig. 2B, we show the average statistics for filopodia growth with the three different standard deviations in the growth rate. The statistics confirm the hunch that variance in the growth rates aids curvature. In Fig. 2B, we also consider the differences in the trajectories when we simulate without any formin torque (lighter colors), versus when the formin exerts a torque at the plus ends. We find that having a nonzero torque leads to fibers with higher average curvature. However, the effect is very slight, which indicates that torque on the fiber endpoint makes little difference when the fibers are fairly straight. Indeed, for straight fibers the translational force induced by twist is zero (see (S2)), so it makes sense that we see little impact on the dynamics in this case.

3.1.3. Dynamic crosslinking alleviates buckling

To understand how the bending behavior depends on the crosslinking turnover rate, we fix $k_{on}/k_{off} = 0.02$, but vary the values of the rates, so that the average number of bound links stays roughly constant (at 8–10 links) while the residence time of the links changes. In Fig. 2C, we show the same simulation of the buckling bundle as in Fig. 2A, but this time with *transient* CLs with off rate $k_{off} = 2.5$/s. We note how dynamic crosslinking alleviates the bending of the peripheral fibers – while the red filament still grows faster than the others, the transient nature of the links prevents it from taking the peripheral filaments with it.

To quantify this effect, we repeat the test of the previous section (with a mean growth rate of 0.5 μm/s and standard deviation of $\sigma = 0.2$ μm/s), but with transient links. Fig. 2D shows that links with longer residence times induce more bending of the filaments. However, even at the longest residence time of 0.4 s ($k_{off} = 2.5$/s), we still observe curvature which is 2 to 3 times smaller than the value for permanent crosslinkers located at the filopodium tip (green lines in Fig. 2B). Thus, transient crosslinkers allow for more variable growth rates without strong bending of the central shaft.

3.2. Motors can effectively braid filaments, aided by transient crosslinking

Whereas Section 3.1 focused on polymerization without motors, in this section we use the five-filament bundle to build intuition about the opposite process: motors without polymerization.

3.2.1. Motors with longer range give efficient braiding and compaction

We now add to the five-filament bundle an external force density that describes the action of helical motors that act near the filopodial boundary (the motors cannot reach the central filament). We begin with the simplest scenario, filaments *without* crosslinkers. In this case, Fig. 3A shows how the action of the motors rapidly twists the fibers into a braid with multiple turns. After the plus end makes about two turns relative to the base, the braiding motion is arrested because fiber elasticity and steric forces balance the motor turning action. The fundamental dynamics of the process are unchanged when we add transient crosslinking, since the motors always tend to drive the filaments into the braid.

How is it possible that the fibers are fully braided (and tightly wound) at the top, when the motors can only reach the outer quarter of the bundle? The explanation (Fig. 3A) is that fibers that reach the motor zone on the outside of the bundle are always getting pushed into the braid by the combination of motor activity (which twists them radially) and inextensibility (which prevents the fibers from stretching), and steric repulsion. Thus, once a fiber gets sufficiently wound, this combination of forces draws it into the braid, even as it loses access to the motors. Note especially the effect of this in the third frame of Fig. 3A, where we see filaments which tend to turn outward initially and are then redirected inward by the motors.

Let us now suppose that the motors can only reach the bottom half of the fibers, i.e., $c_m = 1/2$. In this case (Fig. 3B), the fibers at the bottom again start to form a braid, but, when the top half of the fiber relaxes outward, there is no motor activity to continue the braiding process and the bundle becomes stuck. The final state is a semi-braided state where the fiber endpoints sit roughly 0.2 μm away from the central filament (see endpoint projection in the right of Fig. 3B), which is twice as far as their initial position. Thus motors, while good for twisting and braiding, by themselves typically cannot keep the fiber bundles *compact*.

3.2.2. Transient crosslinking aids compaction

Seeing as the filaments in the top half of the bundle in Fig. 3B appear to be escaping from each other, it makes sense that crosslinking should help keep them together. This is indeed what we see in Fig. 3C, where we introduce transient cross linking (with $k_{off} = 5$/s and $k_{on} = 0.1$/s) into the simulation with motors covering half the length. The endpoint trajectories at the right of Fig. 3C show that the fiber endpoints no longer linearly escape the bundle, so that in the end only one (the red) of the peripheral fibers falls outside of the original boundary. Nevertheless, this process is dependent on having crosslinkers which can turn over fast enough to find and bind pairs of filaments which are on the verge of escape, and is imperfect because eventually the crosslinkers will unbind, and fibers will escape. Thus more transient crosslinking aids compaction, but is not sufficient to keep the bundle compact. While permanent crosslinking at the filament tips is an obvious solution to this problem, Section 3.1.2 hints that having more permanent crosslinkers might lead to more buckling, which decreases compaction. We study this more systematically in Section 3.4, where we give statistics that show an optimum for intermediate crosslink binding times.

3.3. Formins and motors synergize to twist and compress large filopodia

So far, we have discovered that polymerization gives relatively compact bundles of straight filaments, while motor activity gives bent bundles which tend to splay outwards in time. To demonstrate that there is a synergy between motor-driven bending and formin-generated twist, we turn to a larger bundle with 22 fibers (characteristic for filopodia) arranged into four rings (1, 3, 6, and 12 filaments). The rings are spaced 100 nm (the crosslinker rest length) apart, and fibers are positioned with uniform spacing around each ring (Fig. 1C). Starting with this initial geometry, we perform simulations with both motor activity and polymerization. The growth rate of each filament is a random variable which varies in time according to Eq. (1), tuned so that the standard deviation is 0.05 μm/s and the average growth rate of each filament is 0.5 μm/s. We also always distribute the motors in the bottom half of the filopodium, and use dynamic cross linkers with on rate $k_{on} = 0.2$/s and off rate $k_{off} = 10$/s.

What we are interested in is how the motor activity and the torque $N_L = 0.1$ pN $\cdot$ μm that the formin exerts on the fiber tips affect the overall chirality of the bundle. Thus, we will consider three sets of simulations: one with twisting and no motor activity (Fig. 4B), one with motor activity and no twisting (Fig. 4C), and one with both twisting and motor activity (Fig. 4A). These plots show three time points ($t = 0.2$, 0.8, and 2 s); for more time points see the supplementary movies, which show both side views and top views, as well as one movie of all three filopodia growing at once.

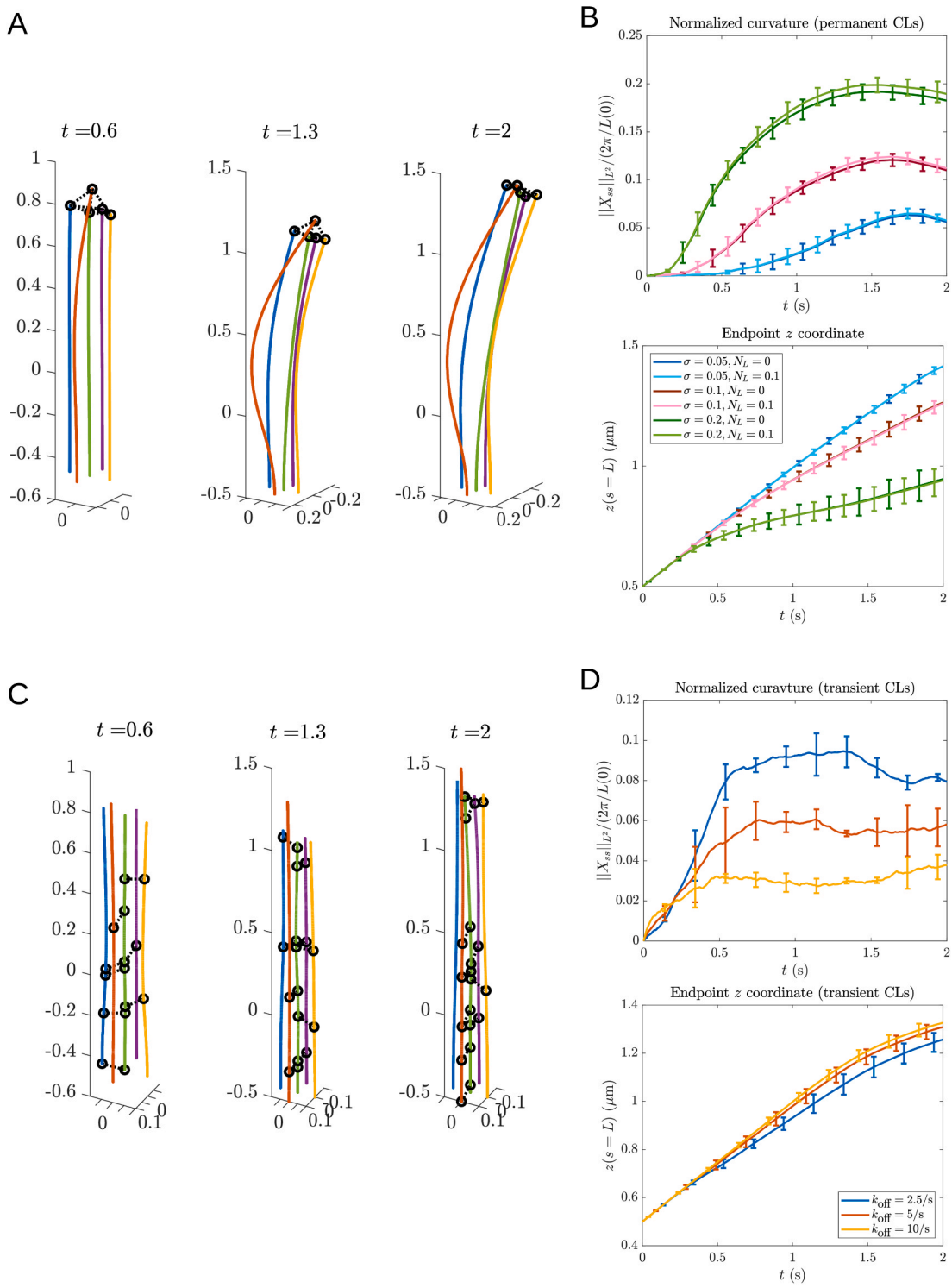

Fig. 2. Lower variance in polymerization rates and dynamic crosslinking alleviate buckling. (A) Simulation of the five-filament bundle with unequal polymerization rates (drawn at $t = 0$ from a normal distribution with mean 0.5 μm/s and standard deviation 0.1 μm/s). Cross links at the tip are permanent in this case, and filaments are color-coded for visualization. (B) Statistics for five-filament filopodial bundle with the tips of the outer filaments permanently crosslinked to the tip of the central filament. The growth rate of each filament is constant in time, but each filament's growth rate is drawn from a normal distribution with mean 0.5 μm/s and varying standard deviation (the values we use are $\sigma = 0.2$, 0.1, and 0.05 μm/s). We plot the average z (in μm) coordinate of the filament endpoints and the average filament curvature (normalized by the curvature of a circle with the same circumference as the filament length) as functions of time (in seconds). We are considering the mean over ten samples, with the error bars showing the standard error of the mean. The lighter colors are when no active torque is applied ($N_L = 0$), while the darker colors show the case when formin at the tip of each growing fiber generates a torque with value $N_L = 0.1$ pN $\cdot$ μm. (C) Simulation of the same bundle as in (A) (with the same growth rates), but with transient cross linkers with off rate $k_{off} = 2.5/s$ (mean residence time 0.4 s). (D) Statistics for five-filament filopodial bundle with transient crosslinkers. We fix $k_{on}/k_{off} = 0.02$, so that the average number of links is roughly constant. Between the simulations, we vary parameter k_{off} (2.5/s – blue curves, 5/s – red curves, and 10/s – yellow curves). We plot the average z (in μm) coordinate of the filament endpoints and the average filament curvature (normalized by the curvature of a circle with the same circumference as the filament length) as functions of time (in seconds). We are considering the mean over ten samples, with the error bars showing the standard error of the mean.

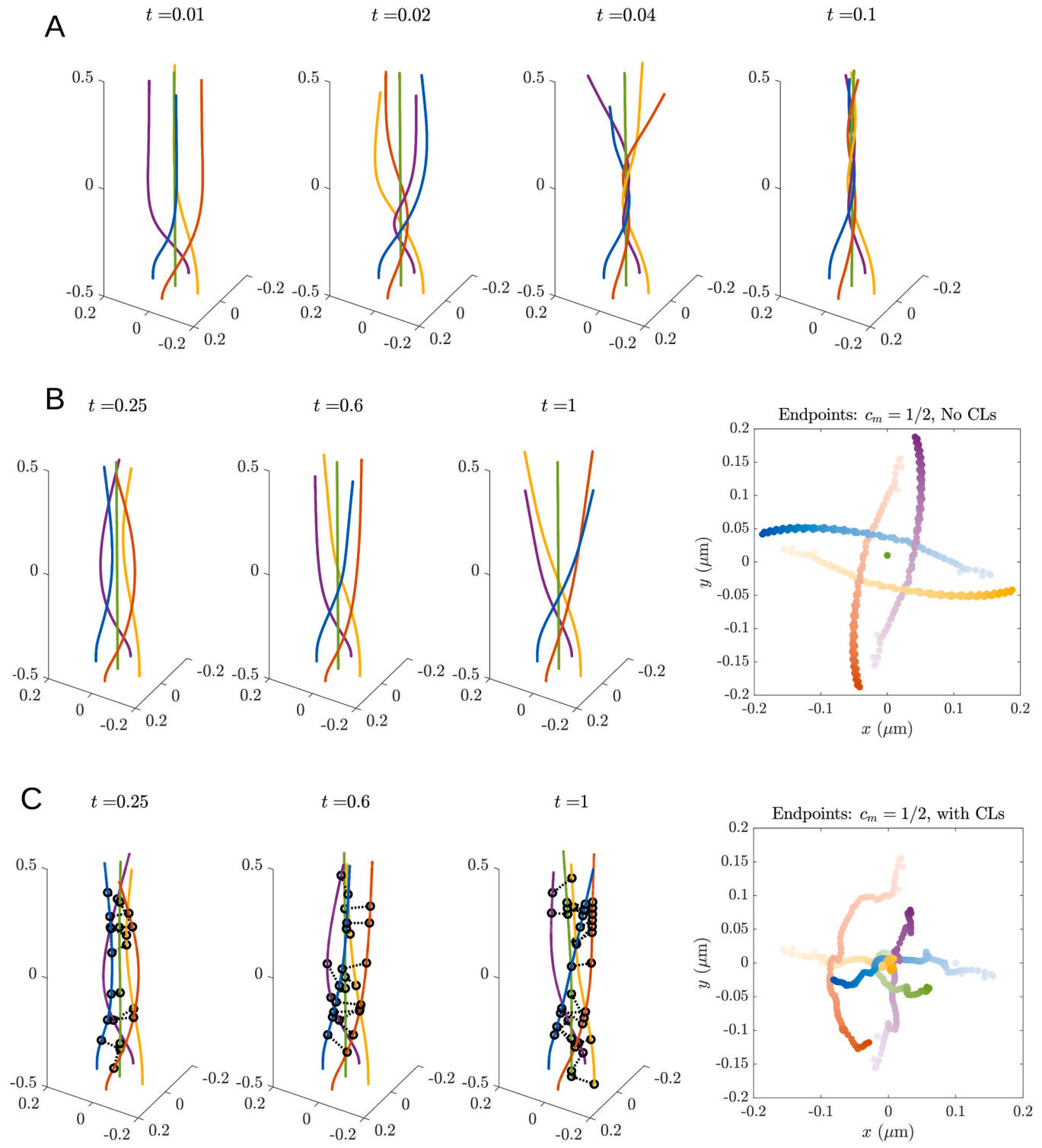

Fig. 3. Motors acting on filopodium edges effectively braid the fibers, but at the cost of loss of compactness. (A) Time sequence of a five-filament "bundle" (no cross links) when the motors act on the edges of the filopodium, and along the whole length of the filaments ($c_m = 1$). Filaments are color-coded for visualization. Time is in seconds, distances are in μm. (B) The same time sequence, but when the motors act only along *half* the length of the fiber ($c_m = 1/2$). The right-most image shows a 2D projection of the fiber endpoints over time. The colors correspond to the fiber colors in the images at left, and darker dots show positions at later time points. (C) Time sequence when motors act along half length of the fiber ($c_m = 1/2$), and transient cross linkers act to keep the bundle compact. The right-most image shows a 2D projection of the fiber endpoints over time. The colors correspond to the fiber colors in the images at left, and darker dots show positions at later time points.

As we already observed in the five-filament case, the twisting of the filaments at the tips makes little difference if there is no motor activity (Fig. 4B). Without motor activity, filaments basically grow straight outward, segregating from time to time into mini-bundles by the crosslinkers, but there is no discernible chirality. When we add motors, but remove twist, we see a braid coming together, but the packing appears fairly loose (Fig. 4C), with filaments growing apart at the top of the bundle, as we already saw in the five-filament case (Section 3.2). By

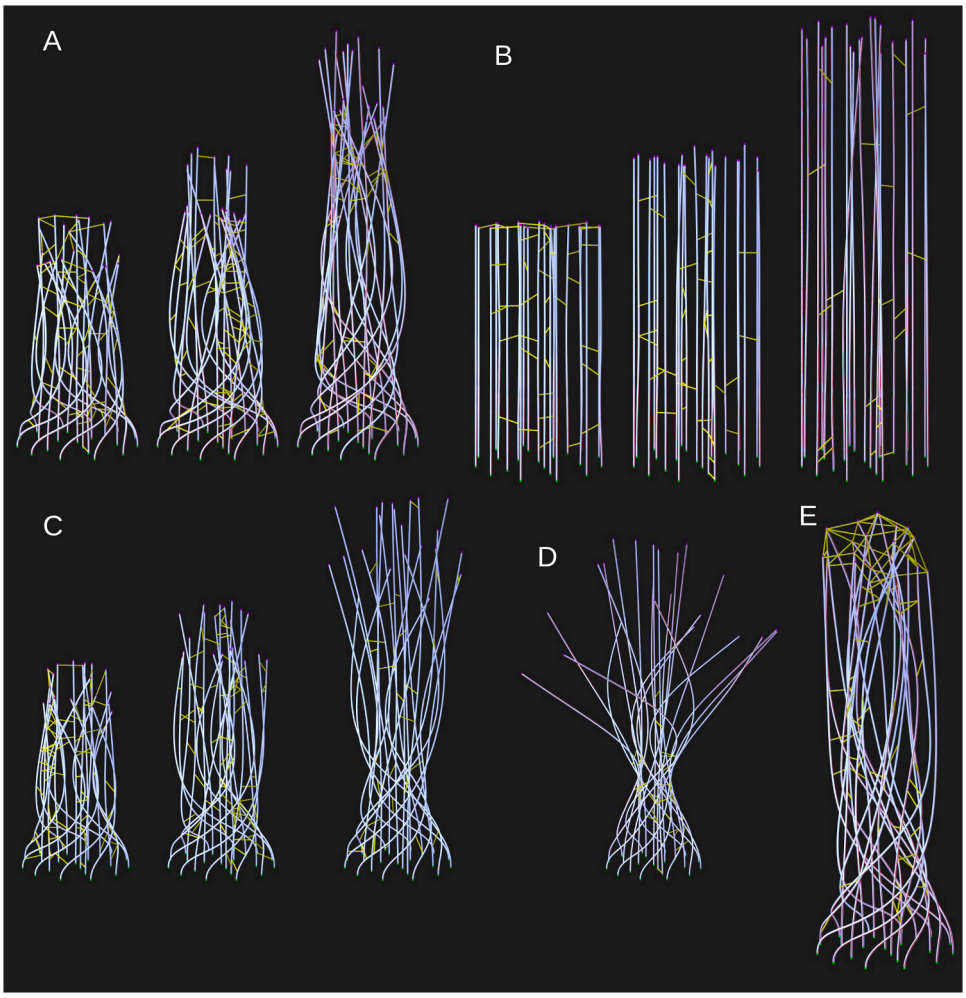

Fig. 4. Snapshots of 22-filament bundles with and without motor and twisting activity, showing that motors and twist synergize to generate a compact bundle. Crosslinks are shown in yellow, filaments in white, and formins in magenta. The green dots show the clamped ends, which represent the branched actin network beneath the filopodium. (A) Time sequence of filopodium growth when there is both formin twisting and motors acting along the half length of the fiber ($c_m = 1/2$). Snapshots are shown at $t = 0.2$, 0.8, and 2 s. See supplementary movie 1 for full sequence. (B) Time sequence of filopodium growth when there is only formin twisting, and no motor activity. Snapshots are shown at $t = 0.2$, 0.8, and 2 s. See supplementary movie 2 for full sequence. (C) Time sequence of filopodium growth when there is only motor activity, and no formin twisting. Snapshots are shown at $t = 0.2$, 0.8, and 2 s. See supplementary movie 3 for full sequence. (D) Snapshot from the end of a simulation ($t = 2$ s) when formins move in the opposite direction (CW, looking from the tip) from the motors (CCW, looking from the tip). See supplementary movie 4 for full sequence. (E) Snapshot from the end of a simulation ($t = 2$ s) when crosslinks at the tip are permanent (a sort of filopodial tip complex; in the simulations, permanent crosslinks connect the plus ends that are the nearest neighbors), while crosslinks below the tip are free to bind and unbind transiently. A less compact bundle with more bending and buckling is observed.

contrast, when we add formin twisting to the motor activity, we see a bundle which is significantly tighter and with filaments that are wound more around the central fiber (Fig. 4A).

3.3.1. *Positive twist at the tip pushes filaments into the center of the filopodium*

To verify that these more compact bundles are not due to random chance, we study the final position (at $t = 2$ s) of the peripheral filament plus ends. In Fig. 5A we plot the endpoints of the outer 12 fibers in the filopodium across ten simulations, projected onto the (x, y) plane. In addition to plotting simulations with CCW formin twist and no motors (blue circles) and motors and no twist (black diamonds), we plot simulations with motor activity and twisting. The red squares show when the formin torque is applied in the same CCW direction as the motors, while the green triangles show the endpoints when the torque is applied in the *opposite* CW direction (Fig. 4D gives an impression of the end position of sample simulations). The significant change from a compact set of the plus ends' ending positions (when the torque is in the same direction) to a very large outward splaying of the plus ends' ending positions (when the torque is in the opposite direction), shows how formin twist in the same (CCW) direction as motor spin is vital in maintaining a tight filopodium shape. Indeed, the filopodium with motors and twist is actually tighter than without motors.

To quantify this effect, we define filopodium compaction as the mean $R = \sqrt{x^2 + y^2}$ coordinate of the peripheral fiber endpoints. We compute the mean across five simulations (60 total fibers), then repeat across the second set of five to generate error bars. Fig. 5B shows how compaction changes when we vary the motor/formin twist model. The colors and shapes of the symbols correspond to those in Fig. 5A; thus, the mean compaction of filopodia with formin twist and no motors is about 0.3, while the compaction for formin twist and motors is roughly 0.15. There is a small but significant increase in R (decrease in compaction) when we introduce motors without the formin twist, on the order of 10–15%. Fig. 5C shows a kind of phase diagram of compaction (R) as a function of the motor force density $f_{\text{mot}}^{(0)}$ and formin twist N_L. As already noted, R is smallest (compaction best) when the formin torque and motor force have the same sign, and worst when they have opposite signs. The

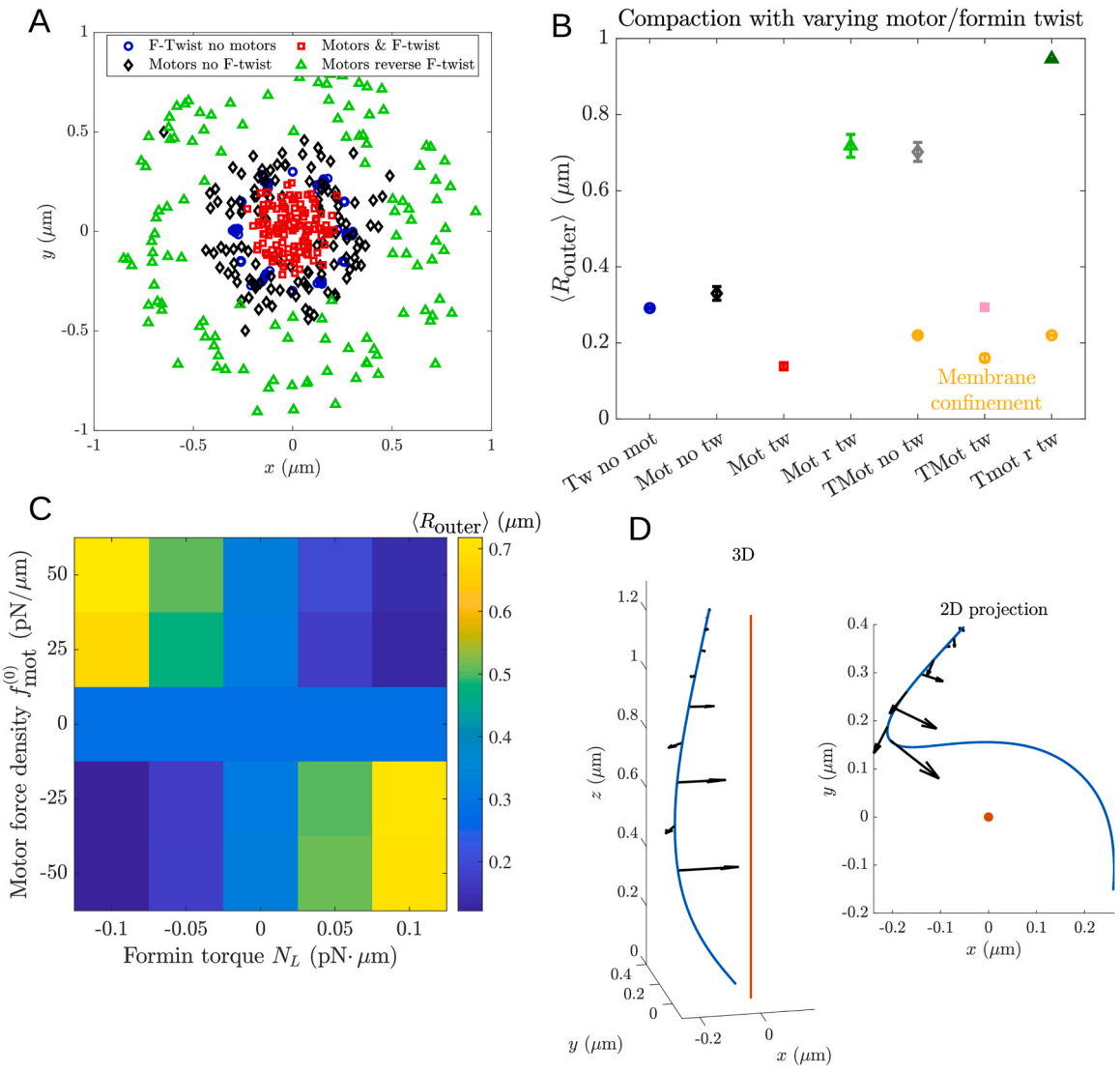

Fig. 5. Compaction is driven by twist forces activated by bending. (A) The positions of the outer 12 filaments' tips at $t = 2$ s, projected onto the (x, y) plane for three simulation conditions. Blue circles correspond to twist without motors, black diamonds correspond to motors without twist, and red squares correspond to motors with twist. The green triangles correspond to what happens when we reverse the direction of formin twisting. Simulations were repeated 10 times for each parameter set. (B) To quantify the data in (A), we define $\langle R_{\text{outer}} \rangle$ as the mean radial coordinate of the endpoints at $t = 2$. Smaller $\langle R_{\text{outer}} \rangle$ then makes for better compaction. We consider simulations with a variety of parameters here. For formins, we use the shorthand "tw" to denote simulations that include CCW formin twist, "no tw" to denote simulations that do not include formin twist, and "r tw" to denote simulations that include CW (reverse) formin twist. For the motors, we use "mot" to denote motors that apply forces, and "TMot" to denote motors with both forces and torques applied to the fibers. For motors with torques, we also plot results that include membrane confinement as yellow circles. See Fig. S9 for more details on this. (C) Phase diagram of $\langle R_{\text{outer}} \rangle$ as a function of formin torque N_L (pN $\cdot$ μm) and motor force density $f^{(0)}_{\text{mot}}$ (pN/μm) (motors only exert force here). Darker blue colors represent better compaction. (D) Shape of an outer filament (in 3D and projection onto the (x, y) plane) in the 22-filament filopodium as computed when the motors apply force to the lower half of the bundle, but without the formin twist. We show the resulting forces on the upper region of the filament (arrows) generated when we apply formin twist and the twist angle assumes its steady state. The red line (circle in the 2D projection) shows the central (z) axis of the filopodium.

compaction appears to depend much more strongly on formin torque than motor force, which indicates that the twist density of the fibers has a strong effect on compaction.

To understand this effect, we isolate a filament *from a simulation without twist* and compute the twist force:

$$\boldsymbol{f}^{(\gamma)} = \gamma \partial_s \left(\psi \left(\partial_s \mathbb{X} \times \partial_s^2 \mathbb{X} \right) \right) = \gamma \psi \left(\partial_s \mathbb{X} \times \partial_s^3 \mathbb{X} \right) \tag{2}$$

when the twist angle $\psi = N_L/\gamma$ is in its constant steady state (this is how the second equality follows from the first). Here γ is the torsional rigidity of actin, N_L is the formin torque, and $\mathbb{X}$ is the 3D curve of the filament centerline (see the SM for details). The fiber and the twist force density on its top half (where motors do not act) are shown in Fig. 5D. There, we see that the twist force is largely directed towards the center of the filopodium, as is qualitatively clear from the large bundle simulations. Equation (2) also shows why the twist force is only significant when motors bend the fibers: the force density is only nonzero when $\partial_s^3 \mathbb{X}$ is nonzero. Thus, when fibers are straight, as is the case when motors are absent, the twist force is zero, and there is no way for the twist to feed back onto the fiber shape. It is necessary for the motors to first bend the fibers, and then formin twist can affect the shape. Thus, the motors and formins synergize to make the bundle more compact.

Given that we need strong bending of the fibers by the motors to activate the twist force, we might expect a decrease in compaction when we decrease the domain of motor activity. In Fig. S4, we show a sample filopodium at $t = 2$ and the corresponding statistics for curvature when

we drop the motor range to the lower 1/4 of the filaments (from 1/2) and outer 1/8 of the circle (from 1/4). We see less bending, and the outward splaying that is characteristic of simulations with insufficient twist force to give contractility (the compaction statistic is $\langle R_{\text{outer}} \rangle = 0.44 \pm 0.02$). Because this effect comes from the fiber curvature and not the formin twist, it is not rescued when we increase the formin twist by a factor of two ($\langle R_{\text{outer}} \rangle = 0.43 \pm 0.02$ for $N_L = 0.2$ pN $\cdot$ μm and the smaller motor range). However, the right panel of Fig. S4 shows that formin twist still draws the filaments inwards, as reversing the direction gives much less compaction ($\langle R_{\text{outer}} \rangle = 0.67 \pm 0.01$ for $N_L = -0.1$ pN $\cdot$ μm and the smaller motor range). Thus the synergy of formin and motors is still there, but its effect is less pronounced when motors do not act as strongly to bend the filaments.

3.3.2. Exploring more realistic helical motor force

In our simplified model of motor forcing, we assume that motors only exert forces in the (x, y) plane perpendicular to the filopodial axis, regardless of the orientation of the filament tangent vector. In reality, motors generate power strokes along the helical path on filaments, and exert forces both tangential to the centerline (towards the base of the fiber) and perpendicular to the centerline. The particular balance of this force is dictated by the type of motor considered; some motors move exactly along the helical pitch of the filament (Norstrom et al., 2010), thus exerting the corresponding ratio of force in the normal to tangential direction. Most motors, however, do not exactly follow this trajectory, sometimes skipping monomers along the filament (Ali et al., 2002b; Tominaga et al., 2003), and consequently have a force which is dominated by the tangential direction. For the case of a motor walking along the helical path, the schematic diagram in Fig. S5 shows how motor activity changes when the filament orientation changes. The left panel shows the filament in blue with its helical path in yellow. The force that the motor exerts is then in the opposite direction of the helical path, and contains a direction both normal and parallel to the filament. In the case when the filament is vertical (tangent vector in the $+z$ direction), then the dominant force is normal to the filament, as we have already implemented. But if the filament orientation changes to become more horizontal (x direction), the dominant motor force becomes more and more downward ($-z$ direction), and there is a corresponding force in the $-x$ direction due to the helicity of the filament. Thus, it is possible that more realistic treatment of the forces might prevent us from accessing the regime where filaments are sufficiently bent to activate twist elasticity.

To explore this, we generalize our procedure for computing motor forces as follows: given a point $\boldsymbol{X}(s)$ on the filament, we compute its cylindrical coordinates (R, θ, z). We then use these coordinates to construct a vector from the filopodial sheath to the filament which points in the inward normal direction, $\boldsymbol{r} = -(\cos\theta, \sin\theta, 0)$. We make this vector orthogonal to the filament by projecting off the tangent vector $\boldsymbol{\tau}(s)$ direction. The motor force then has two components: f_0 in the $\widehat{\boldsymbol{r}}^{\perp}(s) = \widehat{\boldsymbol{r}}(s) \times \boldsymbol{\tau}(s)$ direction, and $3f_0/8$ in the $-\boldsymbol{\tau}(s)$ direction, where the ratio is chosen to match the helical pitch of actin filaments (Dominguez and Holmes, 2011).

We perform a set of simulations with this motor forcing, finding that the integrity of the bundle is completely destroyed (left panel of Fig. S5), because the large downward ($-z$) and compressive ($-\boldsymbol{\tau}$) forces on outer filaments coil them and press to the filopodial base. Actual filopodial architectures do *not* resemble this configuration, and we conclude that the retrograde flow must alleviate these forces. The molecular biophysical basis for this assumption is that the motors are characterized by force-velocity relations, and if a filament moves in the direction of the motor power strokes, then the motor force decreases. We consider two possibilities for the retrograde flow: in the first case, there is a local flow in the $-\boldsymbol{\tau}$ direction on each filament which eliminates the *compressive* force from the motors in the $-\boldsymbol{\tau}$ direction, but not the downward force from the $\widehat{\boldsymbol{r}}^{\perp}(s)$ direction. As shown in the middle frame of Fig. S5, implementing only the force in the $\widehat{\boldsymbol{r}}^{\perp}(s)$ direction (which still changes with the filament orientation) leads to a more ordered bundle, but still causes a significant net downward motion on the outer filaments, such that they coil around the base in the (x, y) plane. If we instead implement a global retrograde flow which cancels the *downward* forces (any forces in the $-z$ direction), we can still retain the compressive forces and get reasonable dynamics, shown in the right panel of Fig. S5. Simply put, these dynamics contain the same assumptions as our original simulations (retrograde flow cancels the force in the $-z$ direction), but have a motor forcing in the planar directions which evolves with the motor geometry.

To test whether the changing motor geometry significantly impacts our results, we consider simulations with the motor forcing $\boldsymbol{f}^{(\text{mot})} = f_0^{(\text{mot})}(\boldsymbol{I} - \widehat{z}\widehat{z})(\widehat{\boldsymbol{r}}^{\perp} - 3/8\boldsymbol{\tau})$, so that the motor force depends on the local filament orientation, but its downward component is attenuated by the retrograde flow. In Fig. S6, we compare the number of rotations around the central filament and the amount of compaction for three different values of the formin twist, finding that the values we obtain are roughly unchanged when we consider this more realistic forcing. Thus, our simplified force model does not impact the overall conclusions, provided that we assume a retrograde flow cancels potentially large downward forces on the filopodium.

3.3.3. Motor torque and deformable membrane

So far, we have neglected the possibility that motors also apply torque to the filament centerlines. Indeed, if the motor action occurs on the fiber boundary rather than the centerline, then motors should exert both a force density and torque density on the fibers. In the SM, Fig. 5B and Figs. S7–S9, we report our results when we repeat the simulations of Section 3.3.1 with the simple change that motor action (along the bottom half of the peripheral fibers) also introduces torque in the same direction as the motor forces (CCW). The result is that the motor torque undoes some of the torque applied by formins, which decreases the amount of compaction for a fixed set of parameters. This makes formin torque all the more vital to prevent extreme outward movement of the filament tips; Fig. 5B shows the compacting effect of formin twist is more drastic in the case when we include motor torque (compare pink square to gray diamond). With formin and motor torque, the radial coordinates of the peripheral filaments are the same at the beginning and end of the simulation (0.3 μm).

Another way to prevent outward motion of the filaments is to confine the filopodial bundle by introducing a deformable membrane. We model this by introducing a normal force which tends to keep the fibers inside of a ring of certain radius. In the SM, Fig. 5B and Fig. S9, we illustrate this effect, the result of which is to introduce a ceiling on the final value of the compaction radius. Fig. 5B (yellow circles) shows that including formin torque still provides additional compaction.

3.4. Role of transient cross linking and variable growth rates

To conclude our study, we return to our original assertion that more permanent crosslinking and more variable growth rates should impact the buckling in the bundle. To study this, we perform the simulations with motor and formin torque, as in Section 3.3.3, but with more variable polymerization rate or slower crosslink dynamics (see details in SM). In Fig. S11, we demonstrate quantitatively that increasing the variance in the fiber growth rate or making the crosslink dynamics slower (see details in SM) leads to increased buckling. We find that, while the trajectories of the outer filaments in the bundle are dominated by the motors and therefore do not change substantially, the inner filaments tend to buckle more under variable growth rates and more permanent crosslinks, in accordance with our observations in Section 3.1. We also find a correlation between buckling and compaction, as compaction tends to correlate with filaments that are *not* buckled, which happens when they all grow at a constant length and have rapidly

exchanging crosslinks.

It is indeed a strange result that transient (rather than permanent) crosslinking aids compaction, since permanent crosslinks should act as an attractive potential between fibers. We found that the relationship is non-monotonic: if there are no crosslinks, the bundles are less compact than both the base parameter value and the value for longer crosslink residence times. Thus when crosslink residence times are too long, the attractive potential can give strange constraints on the trajectories, which leads to buckling and poor compaction. At the opposite end of the spectrum, filaments without crosslinks do have a small outward displacement. There is an optimal crosslink turnover rate when the links are on long enough to promote attraction, but not too long to lead to buckling.

As an example of how permanent crosslinks can constrain fiber trajectories, we consider a simulation where the crosslinks at the fiber plus ends are permanent, mimicking the filopodial tip complex, while crosslinks connecting the filaments' sides can form and break dynamically. Fig. 4E shows the resulting filopodium (without twisting motors, to be consistent with the other plots in Fig. 4). Comparing to Fig. 4A, we observe significantly more bending of the interior fibers and a much wider bundle, as the filopodial tip complex provides an additional constraint preventing the filaments from being drawn into the middle. In addition, the filaments appear more buckled because of the variance in the polymerization rate, and there is a direction of bending to the filopodium, similar to what we saw earlier in five-filament bundles with permanent crosslinks. These qualitative conclusions are confirmed qualitatively in Fig. S12, where we plot the mean curvature and z coordinate in simulations with motor twist and the permanent cross links at the fiber endpoints. Compared to the left panels in Fig. S11, which show the base parameters, the simulations with permanent CLs at the end display more curvature of the inner circles of filaments.

4. Discussion

We found that the spinning action by helical motors effectively "braids" the actin bundle, compacting it, generating buckling, and enhancing the crosslinking. Stochastic fluctuations of actin polymerization rates also contributed to filament buckling and bending of the bundle. Faster turnover of transient crosslinks attenuated the buckling but could enhance coiling and compaction of the bundle. Interestingly, formin-generated twisting alone was much less effective than myosin-generated spinning in inducing filopodial braiding and compaction, but formin action helped the motors to compact the bundle once braided. Indeed, we found that in the absence of confining membrane forces, co-rotating formin action is *necessary* to maintain a compact bundle.

Our model prediction that myosin action, as opposed to formin activity, is the key for coiling the filopodium, is in agreement with the observation that the molecular activities of myosin V and X are involved in rotation of filopodia whereas the formin mDia1 does not play a role in the observed rotations (Leijnse et al., 2022). We note though that formins may not rotate or twist filaments (Kovar and Pollard, 2004), which could be an alternative explanation of why perturbations of formin reported in (Leijnse et al., 2022) did not inhibit the chiral filopodial structure. Another observation from our simulations – that buckling of several filaments that grow faster than others can create an actin loop and respective bulge at the filopodial tip – could be relevant to similar experimentally-observed structures (Li et al., 2023). The mechanisms we discussed here could also be relevant to processes that trigger chiral tilting of actomyosin fibers in adherent cells (Tee et al., 2015). Some of these mechanisms are very similar to microtubule/kinesin interactions generating chirality of the mitotic spindle (Novak et al., 2018).

One of the model predictions – that faster crosslink turnover enhances coiling and compaction in the filopodium – is nontrivial and probably could be tested in future experiments. The two main crosslinkers in filopodia are α-actinin and fascin (Courson and Rock, 2010). Here we tested crosslinking with very rapid kinetics on the scale of several cycles of binding/unbinding per second, which is characteristic of α-actinin (Wachsstock et al., 1994). Another principal crosslinker in filopodia, fascin, has much slower kinetics with the turnover cycle on the scale of 10 s (Aratyn et al., 2007), which implies that the bundle chirality could be sensitive to the concentration ratio between ubiquitous crosslinkers, and could explain why bundle chirality is not universally observed. A simple prediction of the longer residence time is that we should observe more buckling in filopodia crosslinked by fascin compared to α-actinin. Another interesting prediction for the future is that the filopodial bundle chirality is the same as that of the helical myosin motors: if the motors spin filaments CW (CCW), then the bundle will coil CW (CCW), respectively. The predicted effect of formin depends on the relative helicity of the motors and formin: if formin-generated torque rotates filaments in the same direction as the motors, then the bundle will be tighter; if the formin torque is opposite to the motor spinning action, then the bundle will be more disheveled. The most straightforward way to test the model predictions would be (difficult) in vitro experiments, for example growing actin bundles in micro-wells (Colin et al., 2023) with crosslinkers in the solute and with myosins and formins coating different parts of the micro-well surface.

What could be the possible roles of the spinning and twisting actions of the myosins and formins, respectively, and of the resulting coiling and buckling of the filopodial bundles? One very suggestive role, based on the simulations, is the compaction of the bundle, which likely means greater mechanical stability. Mechanical stability of the bundle is, in fact, affected by coiling even without compaction (Daniels and Turner, 2013). Another possibility is that the spinning action could result in rotation of the filopodia around axes not coinciding with bundle axes, as was observed in (Tamada et al., 2010), which could allow filopodia scanning over a greater area around the cell edge. Some filopodia fold back into the cell leading edge and contribute to construction of contractile bundles in the lamella (Nemethova et al., 2008), and in that way pre-established filopodial chirality could trigger larger scale chirality of the cell cortex by interaction with other cytoskeletal structures of the cortex. Coiling and buckling in the filopodial bundle can induce pulling and traction at the tip (Leijnse et al., 2015b). The mechanism of chirality emergence that we explored is but one possibility, and there is likely a diverse inventory of chirality propagation mechanisms, even for just actin bundles. An unknown mechanism, not relying on either myosins or formins, is responsible for a chiral rotation of *Listeria* propelled by a polarized actin tail (Robbins and Theriot, 2003). Turning of long filopodia to the left (Tamada et al., 2010; Li et al., 2023) is not explained by the mechanisms that we considered. General thermodynamic arguments demonstrated that when chiral filaments are bundled, a macroscopic twist is generated in the bundle (Grason and Bruinsma, 2007). It was shown theoretically that crosslink binding to actin filaments along helical patches on the filaments generates intrinsic torques, which wind the bundle superhelically about its central axis (Heussinger and Grason, 2011; Grason, 2015). Recently, a detailed simulation with monomer-scale resolution confirmed that torsional compliance in a finite-width filament can induce chirality in the structure of a crosslinked bundle (Floyd et al., 2022). It was experimentally observed that small rigid actin-binding proteins change the twist of filaments in a concentration-dependent manner, resulting in small, well defined bundle thickness up to 20 filaments (Claessens et al., 2008), which, accidentally or not, is on the order of the filament number in filopodium. Finally, actin bundling by counterions is also predicted to generate chirality (Mohammadinejad et al., 2012).

Adding factors that we ignored in the model will predict even more nontrivial chiral behaviors. These factors include, but are not limited to: 1) mechanical coupling of twisting and bending, even for a single filament (De La Cruz et al., 2010); 2) complex structure and mechanics of the filopodial protein tip complex (Cheng and Mullins, 2020); 3) formin sensing both force and torque during actin filament polymerization (Yu et al., 2017); 4) multi-stack structure of the fast-growing filopodial

bundle (Medalia et al., 2007; Breitsprecher et al., 2011). Inclusion of these factors into the model and scaling up the simulations will allow us to address the open question about how chirality propagates to the cellular (Tee et al., 2015; Zaatri et al., 2021) and multicellular scales (Yashunsky et al., 2022; Tee et al., 2023).

CRediT authorship contribution statement

Mogilner Alex: Writing – review & editing, Writing – original draft, Supervision, Resources, Project administration, Funding acquisition, Formal analysis, Conceptualization. **Maxian Ondrej:** Writing – review & editing, Writing – original draft, Visualization, Software, Methodology, Investigation, Funding acquisition, Formal analysis, Data curation.

Declaration of Competing Interest

The authors have no competing interests to declare.

Data Availability

Code for the simulations is available at the github repository https://github.com/stochasticHydroTools/SlenderBody/tree/master/Matlab/MainPrograms/Filopodium.

Acknowledgements

This work was supported by the National Science Foundation through Research Training Group in Modeling and Simulation under award RTG/DMS-1646339 and through the Division of Mathematical Sciences awards DMS-2052515 and DMS-1953430. Ondrej Maxian was supported by the NSF via GRFP/DGE-1342536, and by the Chicago-Yen fellowship at the University of Chicago. We thank A. Bershadsky for help with literature and fruitful discussions. Code for simulations can be found at https://github.com/stochasticHydroTools/SlenderBody/tree/master/Matlab/MainPrograms/Filopodium.

Appendix A. Supporting information

Supplementary data and movies associated with this article can be found in the online version at doi:10.1016/j.ejcb.2023.151383.

References

Ali, M.Y., Uemura, S., Adachi, K., Itoh, H., Kinosita Jr, K., Ishiwata, S., 2002a. Myosin V is a left-handed spiral motor on the right-handed actin helix. Nat. Struct. Biol. 9 (6), 464–467.
Ali, M.Y., Uemura, S., Adachi, K., Itoh, H., Kinosita Jr, K., Ishiwata, S., 2002b. Myosin v is a left-handed spiral motor on the right-handed actin helix. Nat. Struct. Biol. 9 (6), 464–467.
Alieva, N.O., Efremov, A.K., Hu, S., Oh, D., Chen, Z., Natarajan, M., Ong, H.T., Jégou, A., Romet-Lemonne, G., Groves, J.T., Sheetz, M.P., Yan, J., Bershadsky, A.D., 2019. Myosin IIA and formin dependent mechanosensitivity of filopodia adhesion. Nat. Commun. 10 (1), 3593.
Aratyn, Y.S., Schaus, T.E., Taylor, E.W., Borisy, G.G., 2007. Intrinsic dynamic behavior of fascin in filopodia. Mol. Biol. Cell 18 (10), 3928–3940.
Arjonen, A., Kaukonen, R., Ivaska, J., 2011. Filopodia and adhesion in cancer cell motility. Cell Adh. Migr. 5 (5), 421–430.
Beausang, J.F., Schroeder 3rd, H.W., Nelson, P.C., Goldman, Y.E., 2008. Twirling of actin by myosins II and V observed via polarized TIRF in a modified gliding assay. Biophys. J. 95 (12), 5820–5831.
Berro, J., Michelot, A., Blanchoin, L., Kovar, D.R., Martiel, J.-L., 2007. Attachment conditions control actin filament buckling and the production of forces. Biophys. J. 92 (7), 2546–2558.
Bibeau, J.P., Pandit, N.G., Gray, S., Nejad, N.S., Sindelar, C.V., Cao, W., De La Cruz, E.M., 2023. Twist response of actin filaments. Proc. Natl. Acad. Sci. 120 (4), e2208536120.
Breitsprecher, D., Koestler, S.A., Chizhov, I., Nemethova, M., Mueller, J., Goode, B.L., Small, J.V., Rottner, K., Faix, J., 2011. Cofilin cooperates with fascin to disassemble filopodial actin filaments. J. Cell Sci. 124 (Pt 19), 3305–3318.
Cheney, R.E., O'Shea, M.K., Heuser, J.E., Coelho, M.V., Wolenski, J.S., Espreafico, E.M., Forscher, P., Larson, R.E., Mooseker, M.S., 1993. Brain myosin-v is a two-headed unconventional myosin with motor activity. Cell 75 (1), 13–23.
Cheng, K.W., Mullins, R.D., 2020. Initiation and disassembly of filopodia tip complexes containing VASP and lamellipodin. Mol. Biol. Cell 31 (18), 2021–2034.
Chesarone, M.A., DuPage, A.G., Goode, B.L., 2010. Unleashing formins to remodel the actin and microtubule cytoskeletons. Nat. Rev. Mol. Cell Biol. 11 (1), 62–74.
Claessens, M.M.A.E., Semmrich, C., Ramos, L., Bausch, A.R., 2008. Helical twist controls the thickness of f-actin bundles. Proc. Natl. Acad. Sci. 105 (26), 8819–8822.
Colin, A., Kotila, T., Guérin, C., Orhant-Prioux, M., Vianay, B., Mogilner, A., Lappalainen, P., Théry, M., Blanchoin, L., 2023. Recycling of the actin monomer pool limits the lifetime of network turnover. EMBO J. 42 (9), e112717.
Courson, D.S., Rock, R.S., 2010. Actin cross-link assembly and disassembly mechanics for alpha-actinin and fascin. J. Biol. Chem. 285 (34), 26350–26357.
Daniels, D.R., Turner, M.S., 2013. Islands of conformational stability for filopodia. PLoS One 8 (3), e59010.
Davenport, R.W., Dou, P., Rehder, V., Kater, S.B., 1993. A sensory role for neuronal growth cone filopodia. Nature 361 (6414), 721–724.
De La Cruz, E.M., Roland, J., McCullough, B.R., Blanchoin, L., Martiel, J.-L., 2010. Origin of twist-bend coupling in actin filaments. Biophys. J. 99 (6), 1852–1860.
Dominguez, R., Holmes, K.C., 2011. Actin structure and function. Annu. Rev. Biophys. 40, 169–186.
Evans, L.L., Hammer, J., Bridgman, P.C., 1997. Subcellular localization of myosin V in nerve growth cones and outgrowth from dilute-lethal neurons. J. Cell Sci. 110 (Pt 4), 439–449.
Fierro-González, J.C., White, M.D., Silva, J.C., Plachta, N., 2013. Cadherin-dependent filopodia control preimplantation embryo compaction. Nat. Cell Biol. 15 (12), 1424–1433.
Fletcher, D.A., Mullins, R.D., 2010. Cell mechanics and the cytoskeleton. Nature 463 (7280), 485–492.
Floyd, C., Ni, H., Gunaratne, R.S., Erban, R., Papoian, G.A., 2022. On stretching, bending, shearing, and twisting of actin filaments i: variational models. J. Chem. Theory Comput. 18 (8), 4865–4878.
Forscher, P., Smith, S.J., 1988. Actions of cytochalasins on the organization of actin filaments and microtubules in a neuronal growth cone. J. Cell Biol. 107 (4), 1505–1516.
Grason, G.M., 2015. Colloquium: geometry and optimal packing of twisted columns and filaments. Rev. Mod. Phys. 87 (2), 401.
Grason, G.M., Bruinsma, R.F., 2007. Chirality and equilibrium biopolymer bundles. Phys. Rev. Lett. 99 (9), 098101.
Heussinger, C., Grason, G.M., 2011. Theory of crosslinked bundles of helical filaments: intrinsic torques in self-limiting biopolymer assemblies. J. Chem. Phys. 135 (3), 035104.
Hu, W., Wehrle-Haller, B., Vogel, V., 2014. Maturation of filopodia shaft adhesions is upregulated by local cycles of lamellipodia advancements and retractions. PLoS One 9 (9), e107097.
Inaki, M., Liu, J., Matsuno, K., 2016. Cell chirality: its origin and roles in left-right asymmetric development. Philos. Trans. R. Soc. Lond. B Biol. Sci. 371 (1710).
Jacquemet, G., Hamidi, H., Ivaska, J., 2015. Filopodia in cell adhesion, 3D migration and cancer cell invasion. Curr. Opin. Cell Biol. 36, 23–31.
Jegou, A., Romet-Lemonne, G., 2020. The many implications of actin filament helicity. Semin Cell Dev. Biol. 102, 65–72.
Kovar, D.R., Pollard, T.D., 2004. Insertional assembly of actin filament barbed ends in association with formins produces piconewton forces. Proc. Natl. Acad. Sci. 101 (41), 14725–14730.
Lan, Y., Papoian, G.A., 2008. The stochastic dynamics of filopodial growth. Biophys. J. 94 (10), 3839–3852.
Lebreton, G., Géminard, C., Lapraz, F., Pyrpassopoulos, S., Cerezo, D., Spéder, P., Ostap, E.M., Noselli, S., 2018. Molecular to organismal chirality is induced by the conserved myosin 1D. Science 362 (6417), 949–952.
N. Leijnse, L.B. Oddershede, and P.M. Bendix.Helical buckling of actin inside filopodia generates traction.Proceedings of the National Academy of Sciences, 112(1): 136–141, 2015b.
Leijnse, N., Oddershede, L.B., Bendix, P.M., 2015a. An updated look at actin dynamics in filopodia. Cytoskelet. (Hoboken) 72 (2), 71–79.
Leijnse, N., Barooji, Y.F., Arastoo, M.R., Sønder, S.L., Verhagen, B., Wullkopf, L., Erler, J. T., Semsey, S., Nylandsted, J., Oddershede, L.B., Doostmohammadi, A., Bendix, P.M., 2022. Filopodia rotate and coil by actively generating twist in their actin shaft. Nat. Commun. 13 (1), 1636.
Li, W., Chung, W.-L., Kozlov, M.M., Medalia, O., Geiger, B., Bershadsky, A.D., 2023. Chiral growth of adherent filopodia. Biophys. J. 122 (18), 3704–3721.
Li, X., Chen, B., 2022. How torque on formins is relaxed strongly affects cellular swirling. Biophys. J. 121 (15), 2952–2961.
Linkner, J., Witte, G., Zhao, H., Junemann, A., Nordholz, B., Runge-Wollmann, P., Lappalainen, P., Faix, J., 2014. The inverse BAR domain protein IBARa drives membrane remodeling to control osmoregulation, phagocytosis and cytokinesis. J. Cell Sci. 127 (Pt 6), 1279–1292.
Mallavarapu, A., Mitchison, T., 1999. Regulated actin cytoskeleton assembly at filopodium tips controls their extension and retraction. J. Cell Biol. 146 (5), 1097–1106.
Martiel, J.-L., Michelot, A., Boujemaa-Paterski, R., Blanchoin, L., Berro, J., 2020. Force production by a bundle of growing actin filaments is limited by its mechanical properties. Biophys. J. 118 (1), 182–192.
Mattila, P.K., Lappalainen, P., 2008. Filopodia: molecular architecture and cellular functions. Nat. Rev. Mol. Cell Biol. 9 (6), 446–454.
Maxian, O., Sprinkle, B., Peskin, C.S., Donev, A., 2022. Hydrodynamics of a twisting, bending, inextensible fiber in stokes flow. Phys. Rev. Fluids 7 (7), 074101.
Medalia, O., Beck, M., Ecke, M., Weber, I., Neujahr, R., Baumeister, W., Gerisch, G., 2007. Organization of actin networks in intact filopodia. Curr. Biol. 17 (1), 79–84.
Medeiros, N.A., Burnette, D.T., Forscher, P., 2006. Myosin II functions in actin-bundle turnover in neuronal growth cones. Nat. Cell Biol. 8 (3), 215–226.

Mellor, H., 2010. The role of formins in filopodia formation. Biochim. Biophys. Acta 1803 (2), 191–200.
Mizuno, H., Higashida, C., Yuan, Y., Ishizaki, T., Narumiya, S., Watanabe, N., 2011. Rotational movement of the formin mdia1 along the double helical strand of an actin filament. Science 331 (6013), 80–83.
Mohammadinejad, S., Golestanian, R., Fazli, H., 2012. Chiral structure of f-actin bundle formed by multivalent counterions. Soft Matter 8, 3649–3656.
Naganathan, S.R., Middelkoop, T.C., Fürthauer, S., Grill, S.W., 2016. Actomyosin-driven left-right asymmetry: from molecular torques to chiral self organization. Curr. Opin. Cell Biol. 38, 24–30.
Nemethova, M., Auinger, S., Small, J.V., 2008. Building the actin cytoskeleton: filopodia contribute to the construction of contractile bundles in the lamella. J. Cell Biol. 180 (6), 1233–1244.
Nishizaka, T., Yagi, T., Tanaka, Y., Ishiwata, S., 1993. Right-handed rotation of an actin filament in an in vitro motile system. Nature 361 (6409), 269–271.
Norstrom, M.F., Smithback, P.A., Rock, R.S., 2010. Unconventional processive mechanics of non-muscle myosin iib. J. Biol. Chem. 285 (34), 26326–26334.
Novak, M., Polak, B., Simunić, J., Boban, Z., Kuzmić, B., Thomae, A.W., Tolić, I.M., Pavin, N., 2018. The mitotic spindle is chiral due to torques within microtubule bundles. Nat. Commun. 9 (1), 3571.
Powers, T.R., 2010. Dynamics of filaments and membranes in a viscous fluid. Rev. Mod. Phys. 82 (2), 1607F–1615.
Pronk, S., Geissler, P.L., Fletcher, D.A., 2008. Limits of filopodium stability. Phys. Rev. Lett. 100 (25), 258102.
Robbins, J.R., Theriot, J.A., 2003. Listeria monocytogenes rotates around its long axis during actin-based motility. Curr. Biol. 13 (19), R754–R756.
Sheetz, M.P., Wayne, D.B., Pearlman, A.L., 1992. Extension of filopodia by motor-dependent actin assembly. Cell Motil. Cytoskelet. 22 (3), 160–169.
Shemesh, T., Otomo, T., Rosen, M.K., Bershadsky, A.D., Kozlov, M.M., 2005. A novel mechanism of actin filament processive capping by formin: solution of the rotation paradox. J. Cell Biol. 170 (6), 889–893.
Stump, D.M., 2000. Toroidal supercoiling of writhed rods. Proc. Math. Phys. Eng. Sci. 456 (2000), 1979–1995.
Sun, Y., Sato, O., Ruhnow, F., Arsenault, M.E., Ikebe, M., Goldman, Y.E., 2010. Single-molecule stepping and structural dynamics of myosin X. Nat. Struct. Mol. Biol. 17 (4), 485–491.
Svitkina, T.M., Bulanova, E.A., Chaga, O.Y., Vignjevic, D.M., Kojima, S.-I., Vasiliev, J.M., Borisy, G.G., 2003. Mechanism of filopodia initiation by reorganization of a dendritic network. J. Cell Biol. 160 (3), 409–421.
Tamada, A., Kawase, S., Murakami, F., Kamiguchi, H., 2010. Autonomous right-screw rotation of growth cone filopodia drives neurite turning. J. Cell Biol. 188 (3), 429–441.
Tanaka, Y., Ishijima, A., Ishiwata, S., 1992. Super helix formation of actin filaments in an in vitro motile system. Biochim. Biophys. Acta 1159 (1), 94–98.
Tee, Y.H., Shemesh, T., Thiagarajan, V., Hariadi, R.F., Anderson, K.L., Page, C., Volkmann, N., Hanein, D., Sivaramakrishnan, S., Kozlov, M.M., et al., 2015. Cellular chirality arising from the self-organization of the actin cytoskeleton. Nat. Cell Biol. 17 (4), 445–457.
Tee, Y.H., Goh, W.J., Yong, X., Ong, H.T., Hu, J., Tay, I.Y.Y., Shi, S., Jalal, S., Barnett, S.F. H., Kanchanawong, P., et al., 2023. Actin polymerisation and crosslinking drive left-right asymmetry in single cell and cell collectives. Nat. Commun. 14 (1), 776.
Tominaga, M., Kojima, H., Yokota, E., Orii, H., Nakamori, R., Katayama, E., Anson, M., Shimmen, T., Oiwa, K., 2003. Higher plant myosin xi moves processively on actin with 35 nm steps at high velocity. EMBO J. 22 (6), 1263–1272.
Wachsstock, D.H., Schwarz, W.H., Pollard, T.D., 1994. Cross-linker dynamics determine the mechanical properties of actin gels. Biophys. J. 66 (3), 801–809.
Watanabe, T.M., Tokuo, H., Gonda, K., Higuchi, H., Ikebe, M., 2010. Myosin-X induces filopodia by multiple elongation mechanism. J. Biol. Chem. 285 (25), 19605–19614.
Wood, W., Jacinto, A., Grose, R., Woolner, S., Gale, J., Wilson, C., Martin, P., 2002. Wound healing recapitulates morphogenesis in drosophila embryos. Nat. Cell Biol. 4 (11), 907–912.
Yamada, H., Abe, T., Satoh, A., Okazaki, N., Tago, S., Kobayashi, K., Yoshida, Y., Oda, Y., Watanabe, M., Tomizawa, K., Matsui, H., Takei, K., 2013. Stabilization of actin bundles by a dynamin 1/cortactin ring complex is necessary for growth cone filopodia. J. Neurosci. 33 (10), 4514–4526.
Yashunsky, V., Pearce, D.J.G., Blanch-Mercader, C., Ascione, F., Silberzan, P., Giomi, L., 2022. Chiral edge current in nematic cell monolayers. Phys. Rev. X 12 (4).
Yu, M., Yuan, X., Lu, C., Le, S., Kawamura, R., Efremov, A.K., Zhao, Z., Kozlov, M.M., Sheetz, M., Bershadsky, A., Yan, J., 2017. mdia1 senses both force and torque during f-actin filament polymerization. Nat. Commun. 8 (1).
Zaatri, A., Perry, J.A., Maddox, A.S., 2021. Septins and a formin have distinct functions in anaphase chiral cortical rotation in the Caenorhabditis elegans zygote. Mol. Biol. Cell 32 (14), 1283–1292.
Zhang, H., Berg, J.S., Li, Z., Wang, Y., LÅng, P., Sousa, A.D., Bhaskar, A., Cheney, R.E., Strömblad, S., 2004. Myosin-X provides a motor-based link between integrins and the cytoskeleton. Nat. Cell Biol. 6 (6), 523–531.
Zhao, H., Pykäläinen, A., Lappalainen, P., 2011. I-BAR domain proteins: linking actin and plasma membrane dynamics. Curr. Opin. Cell Biol. 23 (1), 14–21.

Supplemetal Material for Helical motors and formins synergize to compact chiral filopodial bundles: Mathematical and computational models and supplementary figures

Ondrej Maxian[1,3,4] and Alex Mogilner[1,2,*]

[1] *Courant Institute, New York University, New York, NY 10012, USA*

[2] *Department of Biology, New York University, New York, NY 10012, USA*

[3] *Department of Molecular Genetics and Cell Biology, University of Chicago, Chicago, IL 60615, USA*

[4] *Institute for Biophysical Dynamics, University of Chicago, Chicago, IL 60615, USA*

1 Mathematical model of actin filaments and forces

In this work, we model actin filaments as inextensible Euler beams which are subject to bending and twisting forces. The numerical method we choose is based on previous work by some of us [18], which developed a spectral discretization for such filaments. In this section, we summarize our previous work and highlight a few small changes.

We let $\mathbb{X}(s)$ be a parameterization of the filament centerline, and introduce an operator $\boldsymbol{\mathcal{K}}[\mathbb{X}(\cdot)]$ which parameterizes the space of inextensible filament motions. The translational velocity can be written in terms of such motions as

$$\boldsymbol{U}(s) = \boldsymbol{U}_{\text{MP}} + \int_{L/2}^{s} \left(\boldsymbol{\Omega}(s') \times \boldsymbol{\tau}(s')\right) \, ds' := \left(\boldsymbol{\mathcal{K}}[\mathbb{X}(\cdot)]\, \boldsymbol{\alpha}\right)(s) \tag{S1}$$

where $\boldsymbol{U}_{\text{MP}}$ is the velocity of the filament midpoint and $\boldsymbol{\alpha} = (\boldsymbol{\Omega}, \boldsymbol{U}_{\text{MP}})$ represents the translational degrees of freedom. In continuum, the dynamics of the centerline are then governed by the saddle-

point system

$$\begin{pmatrix} -\boldsymbol{\mathcal{M}}_{\mathrm{tt}} & \boldsymbol{\mathcal{K}} \\ \boldsymbol{\mathcal{K}}^* & \mathbf{0} \end{pmatrix} \begin{pmatrix} \boldsymbol{\lambda} \\ \boldsymbol{\alpha} \end{pmatrix} = \begin{pmatrix} \boldsymbol{\mathcal{M}}_{\mathrm{tt}} \left(\boldsymbol{f}^{(\kappa)} + \boldsymbol{f}^{(\gamma)} + \boldsymbol{f}^{(\mathrm{ext})} \right) \\ \mathbf{0} \end{pmatrix}, \tag{S2}$$

$$\text{where} \quad \boldsymbol{f}^{(\kappa)} = -\kappa \partial_s^4 \mathbb{X}, \qquad \boldsymbol{f}^{(\gamma)} = \gamma \partial_s \left(\psi \left(\partial_s \mathbb{X} \times \partial_s^2 \mathbb{X} \right) \right).$$

The first equation says that the total velocity is obtained by multiplying the total force density, which is composed of the constraint force $\boldsymbol{\lambda}$, the bending force $\boldsymbol{f}^{(\kappa)}$, the twisting force $\boldsymbol{f}^{(\gamma)}$, and any external forcing $\boldsymbol{f}^{(\mathrm{ext})}$, by the mobility $\boldsymbol{\mathcal{M}}_{\mathrm{tt}}$. The twisting force $\boldsymbol{f}^{(\gamma)}$ is related to the fiber position $\mathbb{X}$ and the twist density $\psi = \partial_s \theta$, where $\theta(s)$ is the angle of twist of the cross-sectional material frame relative to the twist-free Bishop frame [2]. Here, for simplicitly, we have also neglected the so-called rotation-translation and translation-rotation mobilities [18], which take into account the translational velocity induced by torque and rotational velocity induced by force, so that we only couple twist to translation through the twist force $\boldsymbol{f}^{(\gamma)}$, similar to other studies of rod mechanics [31, 12]. The second equation in (S2), $\boldsymbol{\mathcal{K}}^* \boldsymbol{\lambda} = \mathbf{0}$, enforces the principle of virtual work, which says that the constraint forces $\boldsymbol{\lambda}$ perform no work with respect to all inextensible motions. As discussed in [18, Sec. III(A)], this constraint is equivalent to setting $\boldsymbol{\lambda} = \partial_s \left(T \boldsymbol{\tau} \right)$, for some line tension $T(s)$ [27].

The twist density on the filament centerline evolves via an auxiliary set of equations. The total parallel torque is given by

$$n^{\parallel} = \gamma \partial_s \psi + n^{(\mathrm{ext})}, \tag{S3}$$

where the first term is the parallel torque due to twisting, and the second one represents externally-applied torques (e.g., from motors or crosslinkers). The twist-density ψ then evolves according to the equation

$$\partial_t \psi = \partial_s \Omega^{\parallel} - (\boldsymbol{\Omega} \cdot \partial_s \boldsymbol{\tau}) = \partial_s \Omega^{\parallel} - \left(\boldsymbol{\Omega}^{\perp} \cdot \partial_s \boldsymbol{\tau} \right) \tag{S4}$$

$$\text{where} \quad \Omega^{\parallel} = m_{\mathrm{rr}} \left(n^{\parallel} \boldsymbol{\tau} \right) \cdot \boldsymbol{\tau}, \tag{S5}$$

is the parallel rate of rotation, the perpendicular rate $\boldsymbol{\Omega}$ is obtained from the solution of (S2), and m_{rr} represents the mobility (inverse of drag) relationship between (parallel) torque and (parallel) angular velocity.

Our simulations use a clamped end at the filopodium base ($s = 0$),

$$\mathbb{X}(s=0) = \boldsymbol{X}_0, \qquad \partial_s \mathbb{X}(s=0) = \boldsymbol{\tau}_0, \quad \Omega^{\parallel}(s=0) = 0, \tag{S6}$$

where $\boldsymbol{X}_0$ and $\boldsymbol{\tau}_0$ are the fixed endpoint position and tangent vector, respectively. At the clamped end, we assume that the parallel angular velocity is zero,

$$\Omega^{\parallel}(s=0) = m_{\mathrm{rr}}\gamma\partial_s\psi(0) = 0 \rightarrow \partial_s\psi(0) = 0. \tag{S7}$$

The $s = L$ is more delicate. There, we assume that a clamped formin exerts a fixed *torque* N_L on the fiber,

$$N_L = \gamma\psi(L) \rightarrow \psi(L) = N_L/\gamma, \tag{S8}$$

while the position of the fiber end is free,

$$\partial_s^2\mathbb{X}(s=L) = \mathbf{0}, \quad \partial_s^3\mathbb{X}(s=L) = \mathbf{0}. \tag{S9}$$

Based on (S8), we see that our fixed torque BC is equivalent to formin exerting a fixed twist at the $s = L$ end that is constant in time. At steady state (see Section 2), this corresponds to a constant twist along the fiber, or a constant rotation of the cross section per unit length. Since the twist per unit length is constant, adding length via polymerization then increases the twist angle at the plus (formin-bound) end, meaning that monomers are added at a fixed angle of twist without affecting the rest of the filament [25, 10]. An alternative boundary condition is to assume that formin exerts a fixed *angular velocity* on the $s = L$ end, in which case $\partial_s\psi(L) \equiv \psi_L$. This boundary condition gives no steady state and only specifies twist up to a constant, i.e., it only specifies rotation up to an unknown angle per unit length. For this reason, we reject it as unphysical.

In this work, we are interested in capturing the qualitative behavior of the filaments, but not necessarily the quantitative hydrodynamics. Because of that, we will neglect all hydrodynamic interactions between filaments (and between far-away parts of a single filament), and any coupling between rotation and translation. For the purposes of this study, we only want to capture the qualitative separation of scales between bending and twisting. Because of this, we use the local drag mobilities [22]

$$\boldsymbol{\mathcal{M}}_{\mathrm{tt}}(s) = \frac{\ln\left(\epsilon^{-2}\right)}{8\pi\mu}\left(\boldsymbol{I} + \widehat{\partial_s\mathbb{X}}(s)\widehat{\partial_s\mathbb{X}}(s)\right), \quad m_{\mathrm{rr}} = \frac{1}{4\pi\mu a^2}, \tag{S10}$$

where a is the filament radius and $\epsilon(t) = a/L(t)$ is the filament aspect ratio. Here the translational mobility $\boldsymbol{\mathcal{M}}_{\mathrm{tt}}$ is a 3×3 matrix on each filament point, which expresses the fact that the resistance in the tangential direction is half that in the perpendicular direction. The rotational mobility m_{rr} is a scalar that relates parallel torque $n^{\parallel}$ to rotational velocity $\Omega^{\parallel}$. These mobilities are the minimal number of quantities necessary to capture the separation of scales (twist equilibrates $\mathcal{O}\left(\epsilon^{-2}\right)$-fold faster than force).

Because all quantities are ultimately discrete in simulations, we discretize the continuum curve $\mathbb{X}(s)$ using a set of N_x Chebyshev nodes, which we denote by $\boldsymbol{X}$. These nodes define an interpolating function, which can be used at any point to obtain the position $\mathbb{X}(s)$ (see [17, Sec. 1] or [13, Sec. 6.1] for an explanation of our discretization). Once we have a spatial discretization, the saddle point system (S2) becomes a discrete matrix equation that we solve at each time step. To make our time-marching scheme stable for larger time steps, we treat the bending force implicitly; see [13, Sec. 6.4] for more details.

1.1 Crosslinking

To compute crosslinking forces between pairs of filaments, we use the methodology described in [17, Sec. 6] to transform forces on a grid of uniformly spaced points along the filaments to forces on the Chebyshev grid. The forces can then be converted to the force density $\boldsymbol{f}^{(\mathrm{CL})}$ by multiplying by an inverse weights matrix.

For the uniform points, we resample the filament $\mathbb{X}(s)$ at N_u uniformly-spaced locations, obtaining a vector $\overline{\boldsymbol{X}}$ of sites where crosslinks are bound. The relationship between the two is given by

$$\overline{\boldsymbol{X}} = \boldsymbol{R}^{(u)}\boldsymbol{X} \leftrightarrow \overline{\boldsymbol{X}}_{\{p\}} = \boldsymbol{R}^{(u)}_{\{p,:\}}\boldsymbol{X}, \tag{S11}$$

where $\boldsymbol{R}^{(u)}$ is the resampling matrix and $\boldsymbol{R}^{(u)}_{\{p,:\}}$ is its pth row.

Denoting the uniform points connected by the crosslink with $\overline{\boldsymbol{X}}^{(i)}_{\{p\}}$ and $\overline{\boldsymbol{X}}^{(j)}_{\{q\}}$, we have the displacement

$$\boldsymbol{r} = \overline{\boldsymbol{X}}^{(i)}_{\{p\}} - \overline{\boldsymbol{X}}^{(j)}_{\{q\}} = \boldsymbol{R}^{(u)}_{\{p,:\}}\boldsymbol{X}^{(i)} - \boldsymbol{R}^{(u)}_{\{q,:\}}\boldsymbol{X}^{(j)} \tag{S12}$$

with $r = \|\boldsymbol{r}\|$. Then, let us postulate the crosslink energy and force,

$$\mathcal{E}(r) = \frac{K_c}{2}\left(r - \ell_c\right)^2 \tag{S13}$$

$$\frac{\partial \mathcal{E}}{\partial r} = K_c\left(r - \ell_c\right), \tag{S14}$$

respectively, between the two uniform points, where K_c is the spring constant for the crosslink (units force/length) and ℓ_c is the rest length. The corresponding force on filaments i and j can then be obtained by differentiating the energy

$$\begin{aligned} \boldsymbol{F}^{(i)}_{\{a\}} &= -\frac{\partial \mathcal{E}}{\partial r}\frac{\partial r}{\partial \boldsymbol{X}^{(i)}_{\{a\}}} & \boldsymbol{F}^{(j)}_{\{b\}} &= -\frac{\partial \mathcal{E}}{\partial r}\frac{\partial r}{\partial \boldsymbol{X}^{(j)}_{\{b\}}} \\ \boldsymbol{F}^{(i)}_{\{a\}} &= -\frac{\partial \mathcal{E}}{\partial r}\widehat{\boldsymbol{r}}\boldsymbol{R}^{(u)}_{\{p,a\}} & \boldsymbol{F}^{(j)}_{\{b\}} &= \frac{\partial \mathcal{E}}{\partial r}\widehat{\boldsymbol{r}}\boldsymbol{R}^{(u)}_{\{q,b\}}. \end{aligned} \tag{S15}$$

Note that in the energy (S13), the crosslinks are linear springs that connect to the filaments by flexible joints, so possible bending forces are ignored. Also, the crosslinks bind, effectively, to the 1D contour of a filament, so potential effects from the specific distribution of binding sites along the helical grooves of the filaments are also ignored.

1.1.1 Dynamic crosslinks

To implement dynamic crosslinking, we use a simplified version of the algorithm described in [16]. Each filament is discretized into $N_u = 41$ binding sites. We assume that crosslinkers have rest length ℓ_c, and can stretch at most by a length $\Delta\ell = 2\sqrt{k_B T/K_c}$. Thus, at each time step, we find all pairs of uniform sites on distinct fibers separated by a distance between $\ell_c - \Delta\ell$ and $\ell_c + \Delta\ell$, and assign to each pair a binding rate k_{on} in units of 1/s.[1] We also assign each already bound link an unbinding rate of k_{off}. This gives a set of reactions and rates, which we simulate at each time step using Gillespie's next reaction method [1, 5]. To simplify the algorithm, we assume that unbound links will not rebind in a single time step, and that bound links will not unbind in a single time step. Our previous work had a more detailed model where each end of a crosslinker is distinct; here we simply treat the crosslink as one entity that is bound or unbound.

1.2 Steric forces

We compute steric interaction forces using the method described in [14, Sec. 9.2]. In brief, the steric interaction energy between filaments i and j can be written as

$$\begin{aligned} \mathcal{E}^{(ij)} &= \int_0^L \int_0^L \hat{\mathcal{E}}\left(r\left(s^{(i)}, s^{(j)}\right)\right) ds^{(i)}\, ds^{(j)}, \\ r\left(s^{(i)}, s^{(j)}\right) &= \left\| \mathbb{X}^{(i)}\left(s^{(i)}\right) - \mathbb{X}^{(j)}\left(s^{(j)}\right) \right\|, \end{aligned} \tag{S16}$$

where $\hat{\mathcal{E}}$ is the potential density function

$$\begin{aligned} \hat{\mathcal{E}}(r) &= \frac{\mathcal{E}_0}{a^2} \text{erf}\left(r/(\delta\sqrt{2})\right) \\ \frac{d\hat{\mathcal{E}}}{dr} &= \frac{\mathcal{E}_0}{a^2\delta}\sqrt{\frac{2}{\pi}} \exp\left(-r^2/\left(2\delta^2\right)\right), \end{aligned} \tag{S17}$$

where the Gaussian is truncated at $r_{\max} = 4\delta$, and $\mathcal{E}_0 = 4k_B T$ [26] is the magnitude of the steric force, which leaves $\delta = a$ is the parameter that controls the Gaussian decay.

[1] Technically, the CL on rate should have units of 1/(length×time) to be discretization independent. This is actually complex when the filament length changes in time, so we simply choose a value that gives a characteristic number of engaged crosslinks for a given discretization.

To determine the forces, we compute the double integral (S16) for energy via upsampling the position to a high-resolution Chebyshev grid, then differentiate to get force. Similar to the cross-linking force, we denote the upsampled points via $\overline{\boldsymbol{X}} = \boldsymbol{E}\boldsymbol{X}$. The double integral can then be evaluated and differentiated via

$$\begin{aligned}\mathcal{E} &= \sum_k \sum_j \hat{\mathcal{E}}\left(\left\|\overline{\boldsymbol{X}}_{\{k\}} - \overline{\boldsymbol{X}}_{\{j\}}\right\|\right) w_k w_j \qquad \text{(S18)}\\ &= \sum_k \sum_j \hat{\mathcal{E}}\left(\left\|\boldsymbol{E}_{kp}\boldsymbol{X}_{\{p\}} - \boldsymbol{E}_{jq}\boldsymbol{X}_{\{q\}}\right\|\right) w_k w_j\end{aligned}$$

$$\boldsymbol{F}^{(i)}_{\{a\}} = -\frac{\partial \mathcal{E}}{\partial \boldsymbol{X}^{(i)}_{\{a\}}} = -\sum_k \sum_j \frac{\partial \hat{\mathcal{E}}}{\partial r}(r_{kj})\,\widehat{\boldsymbol{r}}_{kj}\boldsymbol{E}_{ka} w_k w_j. \qquad \text{(S19)}$$

The last equation gives the force at Chebyshev node a on filament i, and is a function of the integration weights w_k and w_j of points k and j on the upsampled grid. In this work, we use $N_u = 101$ upsampling points to compute the steric forces on the filaments, and the points we choose are at arclength coordinates $s = 0, \Delta s_u, \ldots, L$, where $\Delta s_u = L/(N_u - 1)$ is the spacing. The corresponding weights are $w = \Delta s_u/2, \Delta s_u, \ldots \Delta s_u, \Delta s_u/2$, so that the first and last point have a weight of $1/2$, in accordance with the trapezoid rule. Note that the sum (S19) can be computed efficiently via a neighbor search (`rangesearch` in Matlab).

1.3 Numerical method for polymerization

To model linear polymerization of a filament $\mathbb{X}(s)$ at the $s = L$ end, we use the following algorithm:

1. Sample the Chebyshev interpolants $\mathbb{X}(s = L)$ and $\partial_s \mathbb{X}(s = L)$ to obtain the position and tangent vector at $s = L$. Let $\boldsymbol{X}_L$ denote the position and $\boldsymbol{\tau}_L$ denote the normalized tangent vector.

2. Add an additional point to the matrix of Chebyshev nodes,

$$\widetilde{\boldsymbol{X}} = \begin{pmatrix} \boldsymbol{X} \\ \boldsymbol{X}_L + L'(t)\Delta t \boldsymbol{\tau}_L \end{pmatrix}. \qquad \text{(S20)}$$

3. Reparameterize the filament by its new length. That is, the new set of evaluation points in s is given by $\widetilde{\boldsymbol{s}} = (\boldsymbol{s}, L + L'(t)\Delta t)/(L + L'(t)\Delta t)$ and goes from zero to one.

4. Let $\boldsymbol{R}$ be the matrix that evaluates the Chebyshev interpolant defined by the arclength points $\boldsymbol{s}$ at $\widetilde{\boldsymbol{s}}$. Then set $\boldsymbol{X} = \boldsymbol{R}^{\dagger}\widetilde{\boldsymbol{X}}$ to obtain the positions at the Chebyshev nodes at the next time step. This resamples the filament at the nodes $\boldsymbol{s}$, but in the new parameterization.

5. The parameter s is no longer an arclength parameter, but is the distance in *reference arclength* coordinates. The new arclength parameter is given by

$$s^*(s,t) = L(t)/L(0)s.$$

Thus, at the next time step, we can solve all the equations in coordinates of Section 1 via the transformation $\partial/\partial s^* = (L_0/L(t))\,\partial/\partial s$, i.e., by scaling all differentiation and integration operations appropriately.

We note that a similar reparameterization algorithm was employed in [20, Sec. 2.5] to model polymerization. However, in that work, the authors used the chain rule to write

$$\partial_t \mathbb{X} = \partial_t \mathbb{X}|_{s^*} + s\frac{L'(t)}{L(t)}\partial_s \mathbb{X}, \tag{S21}$$

so that the first term can be obtained using an inextensible algorithm, and the second term added on afterwards. We found this formulation to be highly unstable numerically because each point locally extends in a direction according to its tangent vector. Because of this, numerical instabilities in tangent vector directions tend to be amplified. Our approach is more physical, because it models the addition of monomers at the $s = L$ end, which happens along the direction corresponding to the last tangent vector. As (S21) suggests, we also first solve the equations of Section 1 to evolve the filament positions (inextensible in the s^* coordinate frame), then add the polymerization at the end of the time step.

1.4 Parameters

Throughout this study, we use the parameters in Table 1.

Parameter	Definition	Value	Notes/Reference
κ	Filament bending modulus	0.068 pN·μm^2	Bend persistence length = 17 μm [6]
γ	Filament twist modulus	0.041 pN·μm^2	Twist persistence length = 10 μm [3]
a	Filament radius	4 nm	[7]
L	Filament length	1–2 μm	For nascent filopodia [9]
ℓ_c	Crosslink rest length	100 nm	[15, 16]
K_c	Crosslink stiffness	100 pN/μm	[15, 16]
N_L	Formin torque	0.1 pN· μm	[10]
μ	Suspending fluid viscosity	1 Pa·s	[11]
k_BT	Thermal energy	4.1×10^{-3} pN·μm	
k_{on}	Crosslinker on rate	0.05–0.2 s^{-1}	Chosen to give characteristic # of CLs
k_{off}	Crosslinker off rate	2.5–10 s^{-1}	[29]
$f_0^{(\text{mot})}$	Motor force magnitude	50 pN/μm	estimated from the data of [19, 28]
$\dot{L}$	Actin polymerization rate	0.5 μm/s	Mean value; estimated from [8]
N	Number of tangent vectors	20	
Δt	Time step size	$[5 \times 10^{-5}, 2 \times 10^{-4}]$ s	

Table 1: Parameters for our simulation study.

2 Formin-generated twist and supercoiling

This section provides a linear stability analysis of the behavior that leads to actin supercoiling. Because twist equilibrates much faster than bending, we can say that the twist evolution equation (S4) is in a steady state, so that it obeys the two-point boundary value problem

$$\partial_s^2 \psi = 0 \qquad \partial_s \psi(0) = 0 \qquad \psi(L) = N_L/\gamma. \tag{S22}$$

This boundary value problem has the obvious solution

$$\psi \equiv \psi(L) = N_L/\gamma, \tag{S23}$$

for the twist profile. The constant twist (S23) implies that the angle of rotation of the fiber $\theta = \int \psi(s)\, ds = \psi s$, is linear along the fiber.

Armed with this, we can perform a stability analysis on the fiber evolution equation. To do this, we linearize the evolution equation (S2) around a straight fiber $\mathbb{X}_0(s) = (0, 0, s)$, then substitute the constant ψ from (S23). Setting $\mathbb{X} = \mathbb{X}_0 + \delta\mathbb{X}^\perp$, where $\delta\mathbb{X}$ is a *perpendicular* perturbation, we get the linearized dynamics (to first order in δ in the perpendicular direction)

$$\partial_t \mathbb{X}^\perp = \frac{\ln\left(\epsilon^{-2}\right)}{8\pi\mu}\left(-\kappa\partial_s^4\mathbb{X}^\perp + \gamma\psi\left(\partial_s\mathbb{X}_0 \times \partial_s^3\mathbb{X}^\perp\right)\right). \tag{S24}$$

We now follow the technique of [31] by mapping $\mathbb{X}^\perp = (X, Y, \sim)$ to the complex plane, so that the complex number $h = X + iY$ represents the degrees of freedom, and $\partial_s\mathbb{X}_0 \times \partial_s^3\mathbb{X}^\perp = i\partial_s^3 h$. The transformed evolution equation (S24) becomes

$$\partial_t h = \frac{\ln\left(\epsilon^{-2}\right)}{8\pi\mu}\left(-\kappa\partial_s^4 h + i\gamma\psi\partial_s^3 h\right). \tag{S25}$$

For linear stability analysis, we set $h(s,t) = e^{\omega t}\xi(s)$, which gives the two point eigenvalue problem

$$\omega\xi = \frac{\ln\left(\epsilon^{-2}\right)}{8\pi\mu}\left(-\kappa\xi^{(4)} + i\gamma\psi\xi'''\right) \tag{S26}$$
$$\xi''(0,L) = 0 \qquad \xi'''(0,L) = 0.$$

Our goal here is to find ψ such that the perturbation is linearly unstable. Similar to [31], we expect that, at the critical $\psi = \psi_{\text{crit}}$, the twisting torque $\sim \gamma\psi$ will be equal to the bending torque $\sim \kappa/L$. As such, we look for a critical value of $\psi_{\text{crit}} = c\kappa/(L\gamma)$ such that there exists an eigenvalue ω in (S26) with positive real part. This can be done numerically using Chebfun [21, 4], an open-source software for numerical computation with functions, which gives

$$\psi_{\text{crit}} \approx 1.41\frac{2\pi}{L}\frac{\kappa}{\gamma}. \tag{S27}$$

Converting this to a number of turns, we find that $N_{\mathrm{t,crit}} = L\psi_{\mathrm{crit}}/(2\pi) = 1.41(\kappa/\gamma)$. For actin filaments, $\kappa \approx 17$ pN$\cdot\mu$m^2 [6], while $\gamma \approx 10$ pN$\cdot\mu$m^2 [3]. This gives a critical number of turns $N_{\mathrm{t,crit}} = 2.4$ for actin filaments of given length. If a filament is twisted less than that, it remains straight; if it is twisted more, it supercoils.

A similar stability analysis to the one here was also conducted for a clamped filament being spun at one end [31], and a twisted closed loop [30, 24].

3 Supplemental modeling results

3.1 Motor torque

If the motor action occurs on the fiber boundary rather than the centerline, then motors should exert both a force density $f^{(0)}_{\mathrm{mot}}$ and torque density $n_m = f^{(0)}_{\mathrm{mot}}a$ on the fiber. It is helpful to first consider how the torque by motors changes the profile of twist on the peripheral fibers. When the motors apply a torque along the bottom half of the fiber, they rotate the filament cross section there in the same direction as formin. Fig. S7 shows the effect of this over time; the angle of rotation at the bottom of the filopodium becomes more and more positive, which means the twist becomes more negative, and is no longer constant along the centerline. Thus, while the twist remains positive at the tip in accordance with the boundary condition induced by formin, the effect of the motor torque is to *reduce* the twist along the rest of the fiilament. Fig. S8 shows that changing the torque induced by formin simply shifts the endpoint/boundary condition for twist at the plus end. Our expectation is therefore that twist from motors will make twist more negative, which will reduce the force driving the fibers inward. This is indeed the case; as shown in Fig. 5B, the amount of compaction in simulations with motor twist is always less than for simulations that do not include motor torque, and the least compact bundle is one with reverse formin twist and CCW motor torque.

3.2 Confining membrane as a cap on outward growth

We mostly simulate the simpler case of the motors acting on the filopodial bundle from a rigid cylindrical filopodial sheath. Here we consider, approximately, the case of deformable membrane by following the formalism in [23]. The mechanical energy of the cylindrical membrane envelope around the filopodial bundle (of radius R and length L) is equal to $E = L[(\pi\kappa/R) + 2\pi\gamma R]$. Here κ is the membrane rigidity ($\kappa \sim 10k_BT$), and γ is the membrane tension ($\gamma \sim 0.001k_BT/\mathrm{nm}^2$).

This energy reaches minimum at given L for radius $R_0 = \sqrt{\kappa/2\gamma}$ ∼100 nm. At this radius, the cylindrical walls of the membrane do not exert any inward force on the actin bundle. Also, the absence of buckling by the membrane (which tries to decrease L and therefore exerts some potentially buckling force) was shown in [23]. Let us consider the case when the radius is greater than R_0. Then, approximately, the bending term in the membrane energy can be neglected, and the membrane tension is opposed by the elastic force from deforming the 12 outer filaments of the filopodial bundle. By the Laplace Law, the effective outward pressure from the filament bundle onto the circumference of the membrane cylinder, per unit length of the membrane cylinder, is equal to $P = \gamma/R$. Thus, the force per filament, per unit length of the filament, is $f = 2\pi RP/12 \sim \gamma/2 \sim 0.0005 k_B T/\text{nm}^2 \sim 1\text{pN}/\mu\text{m}$. Computing the force accurately requires numerically minimizing the elastic energy of the bundle together with mechanical energy of the membrane, but these are very involved numerical calculations [23], so here we limit the analysis to using an approximate constant restraining force from the membrane.

Therefore, to simulate membrane confinement, we add a force proportional to the inward normal vector at each filament point $\boldsymbol{n}(s) = (-\cos(\theta(s)), -\sin(\theta(s)), 0)$ in the region where the motors act (the outer 1/4 of the filopodium, defined by the initial configuration; see Section 2 for the definition of $\theta(s)$). This corresponds to any radial coordinates exceeding 225 nm. In Fig. S9, we show the results of simulations with membrane force, in particular the endpoint positions of the peripheral filaments, projected onto the xy plane in the same way as Fig. 5A. We observe significantly more compaction when the confinement force is included, regardless of the value of formin torque. Interestingly, simulations with no formin torque or reverse formin torque show that the endpoints form a tight circle of radius approximately 225 nm (which is the beginning of the confining region), which suggests that membrane forces in this case provide a "ceiling" on the expansion of the bundlle. By contrast, when formin torque is in the same direction as motors, the synergistic effect is again observed, and the endpoints position themselves anywhere from 0 to 0.2 in radial coordinates. We quantify this by adding to Fig. 5B the mean outer radius when membrane forces are included (yellow circles on the plot). There we see that, even with the extra confinement, the radial coordinates with formin torque in the proper direction are still about 30% lower than those with no formin torque or formin torque in the reverse direction. Thus the synergistic effect of formin and motors is still present, but reduced by the membrane providing a cap on outward displacement.

3.3 Role of transient cross linking and variable growth rates

To study the effect of cross-linking and growth rates, we perform the same sets of simulations as in Section 3.3.3 (i.e., with motor and formin torque), but with the polymerization rate four times more variable (standard deviation 0.2 μm/s) or the crosslink dynamics four times as slow ($k_{\text{on}} = 0.05$/s, $k_{\text{off}} = 2.5$/s). Unlike in simulations with five fibers, here we expect the location of a fiber (in terms of which ring it sits in) to be important for determining the statistics of its motion (since, e.g., motors can only act along the outer 25% of the bundle, which means they can only act along the outer circle of fibers initially). In Figs. S10–S12, we therefore segregate our statistics by ring or circle, showing the central fiber in blue, the smaller circle of 3 fibers in red, the middle circle of 6 fibers in yellow, and the largest outer circle of 12 fibers in purple.

Our first observation is in Fig. S10, where we show the number of rotations each circle of fibers makes around the central fiber in simulations that include (left) formin twist and simulations that do not (right). We see little change in the trajectory of the *midpoints* in this case, but a significant increase in the number of rotations the *inner circle endpoints* make around the central fiber. The increase in rotation comes from the tightening of the bundle in the formin twist case. When the bundle is tighter at the top, more crosslinks can bind the top halves of interior fibers to the rotating outer fibers, increasing the overall rotation of the inner ring. Indeed, the average number of crosslinks is increased by roughly 20% (from 45.3 ± 0.3 to 52.2 ± 0.1) when we account for formin twist.

Similar to the five-filament bundle, we find that increasing the variance in the fiber growth rate or making the crosslink dynamics slower both lead to increased buckling in fiber positions. To demonstrate this quantitatively, we perform a set of simulations with motor and formin torque, but increase the polymerization rate variance from 0.05 to 0.2 (for more variable growth rate), or decrease the crosslink on and off rates by a factor of 4 (to $k_{\text{on}} = 0.05$/s and $k_{\text{off}} = 2.5$/s). In Fig. S11, we plot the mean L^2 curvature and z coordinate of each circle of filaments. We find that, while the trajectories of the outer filaments are dominated by the motors and therefore do not change substantially, the inner filaments tend to buckle more under variable growth rates and more permanent crosslinks, in accordance with our observations in Section 3.1. We also find a correlation between buckling and compaction, as might be expected from the five-filament visual in Fig. 2A: the mean radius of the outer filaments is 0.29 ± 0.01 for the base parameters, 0.32 ± 0.06 for the more variable growth rate, and 0.38 ± 0.05 for the slower CLs. We found that the relationship

between crosslinking and compaction is non-monotonic: if there are no crosslinks, the compaction is 0.44 ± 0.01, which is less compact than both the base parameter value and the value for longer crosslink residence times.

Movie legends: Movies of 22-filament bundles with and without motor and twisting activity, showing that motors and twist synergize to generate a compact bundle. Crosslinks are shown in yellow, filaments in white, and formins in magenta. The green dots show the clamped ends, which represent the branched actin network beneath the filopodium. The left side of the movie shows a side view, while the right side shows a top view (in this case, the filaments appear to move outward because of the perspective of the observer).

Movie 1: CCW Motors and CCW formin twisting.

Movie 2: No motors, but CCW formin twisting.

Movie 3: CCW Motors, but no formin twisting.

Movie 4: CCW Motors, with CW formin twisting (opposite direction).

References

[1] David F Anderson. A modified next reaction method for simulating chemical systems with time dependent propensities and delays. *The Journal of chemical physics*, 127(21):214107, 2007.

[2] Miklós Bergou, Max Wardetzky, Stephen Robinson, Basile Audoly, and Eitan Grinspun. Discrete elastic rods. In *ACM SIGGRAPH 2008 papers*, pages 1–12. 2008.

[3] Jeffrey P Bibeau, Nandan G Pandit, Shawn Gray, Nooshin Shatery Nejad, Charles V Sindelar, Wenxiang Cao, and Enrique M De La Cruz. Twist response of actin filaments. *Proceedings of the National Academy of Sciences*, 120(4):e2208536120, 2023.

[4] Tobin A Driscoll, Nicholas Hale, and Lloyd N Trefethen. Chebfun guide, 2014.

[5] Daniel T Gillespie. Stochastic simulation of chemical kinetics. *Annu. Rev. Phys. Chem.*, 58:35–55, 2007.

[6] Frederick Gittes, Brian Mickey, Jilda Nettleton, and Jonathon Howard. Flexural rigidity of microtubules and actin filaments measured from thermal fluctuations in shape. *The Journal of cell biology*, 120(4):923–934, 1993.

[7] Enrico Grazi. What is the diameter of the actin filament? *FEBS letters*, 405(3):249–252, 1997.

[8] Yueheng Lan and Garegin A Papoian. The stochastic dynamics of filopodial growth. *Biophys. J.*, 94(10):3839–3852, May 2008.

[9] Natascha Leijnse, Younes Farhangi Barooji, Mohammad Reza Arastoo, Stine Lauritzen Sønder, Bram Verhagen, Lena Wullkopf, Janine Terra Erler, Szabolcs Semsey, Jesper Nylandsted, Lene Broeng Oddershede, Amin Doostmohammadi, and Poul Martin Bendix. Filopodia rotate and coil by actively generating twist in their actin shaft. *Nat. Commun.*, 13(1):1636, March 2022.

[10] Xi Li and Bin Chen. How torque on formins is relaxed strongly affects cellular swirling. *Biophysical Journal*, 121(15):2952–2961, 2022.

[11] Katherine Luby-Phelps. Cytoarchitecture and physical properties of cytoplasm: volume, viscosity, diffusion, intracellular surface area. In *International review of cytology*, volume 192, pages 189–221. Elsevier, 1999.

[12] Yi Man, William Page, Robert J Poole, and Eric Lauga. Bundling of elastic filaments induced by hydrodynamic interactions. *Physical Review Fluids*, 2(12):123101, 2017.

[13] Ondrej Maxian. *Hydrodynamics of Transiently Cross-Linked Actin Networks: Theory, Numerics, and Emergent Behaviors*. PhD thesis, New York University, 2023.

[14] Ondrej Maxian. *Hydrodynamics of transiently cross-linked actin networks: theory, numerics, and emergent behaviors*. PhD thesis, New York University, 2023.

[15] Ondrej Maxian, Aleksandar Donev, and Alex Mogilner. Interplay between brownian motion and cross-linking controls bundling dynamics in actin networks. *Biophysical journal*, 121(7):1230–1245, 2022.

[16] Ondrej Maxian, Raul P Peláez, Alex Mogilner, and Aleksandar Donev. Simulations of dynamically cross-linked actin networks: morphology, rheology, and hydrodynamic interactions. *PLOS Computational Biology*, 17(12):e1009240, 2021.

[17] Ondrej Maxian, Brennan Sprinkle, and Aleksandar Donev. Bending fluctuations in semiflexible, inextensible, slender filaments in stokes flow: towards a spectral discretization. *arXiv preprint arXiv:2301.11123*, 2023.

[18] Ondrej Maxian, Brennan Sprinkle, Charles S Peskin, and Aleksandar Donev. Hydrodynamics of a twisting, bending, inextensible fiber in stokes flow. *Physical Review Fluids*, 7(7):074101, 2022.

[19] K E Miller and M P Sheetz. Characterization of myosin V binding to brain vesicles. *J. Biol. Chem.*, 275(4):2598–2606, January 2000.

[20] Ehssan Nazockdast, Abtin Rahimian, Denis Zorin, and Michael Shelley. A fast platform for simulating semi-flexible fiber suspensions applied to cell mechanics. *J. Comput. Phys.*, 329:173–209, 2017.

[21] Rodrigo B Platte and Lloyd N Trefethen. Chebfun: a new kind of numerical computing. In *Progress in industrial mathematics at ECMI 2008*, pages 69–87. Springer, 2010.

[22] Thomas R Powers. Dynamics of filaments and membranes in a viscous fluid. *Reviews of Modern Physics*, 82(2):1607F–1615, 2010.

[23] Sander Pronk, Phillip L Geissler, and Daniel A Fletcher. Limits of filopodium stability. *Phys. Rev. Lett.*, 100(25):258102, June 2008.

[24] T Sanchez, IM Kulic, and Z Dogic. Circularization, photomechanical switching, and a supercoiling transition of actin filaments. *Physical review letters*, 104(9):098103, 2010.

[25] Tom Shemesh, Takanori Otomo, Michael K Rosen, Alexander D Bershadsky, and Michael M Kozlov. A novel mechanism of actin filament processive capping by formin: solution of the rotation paradox. *The Journal of cell biology*, 170(6):889–893, 2005.

[26] Brennan Sprinkle, Ernest B Van Der Wee, Yixiang Luo, Michelle M Driscoll, and Aleksandar Donev. Driven dynamics in dense suspensions of microrollers. *Soft Matter*, 16(34):7982–8001, 2020.

[27] Anna-Karin Tornberg and Michael J Shelley. Simulating the dynamics and interactions of flexible fibers in stokes flows. *Journal of Computational Physics*, 196(1):8–40, 2004.

[28] Sotaro Uemura, Hideo Higuchi, Adrian O Olivares, Enrique M De La Cruz, and Shin'ichi Ishiwata. Mechanochemical coupling of two substeps in a single myosin V motor. *Nat. Struct. Mol. Biol.*, 11(9):877–883, September 2004.

[29] D H Wachsstock, W H Schwarz, and T D Pollard. Cross-linker dynamics determine the mechanical properties of actin gels. *Biophys. J.*, 66(3):801–809, March 1994.

[30] Charles W Wolgemuth, Raymond E Goldstein, and Thomas R Powers. Dynamic supercoiling bifurcations of growing elastic filaments. *Physica D: Nonlinear Phenomena*, 190(3-4):266–289, 2004.

[31] Charles W Wolgemuth, Thomas R Powers, and Raymond E Goldstein. Twirling and whirling: Viscous dynamics of rotating elastic filaments. *Physical Review Letters*, 84(7):1623, 2000.

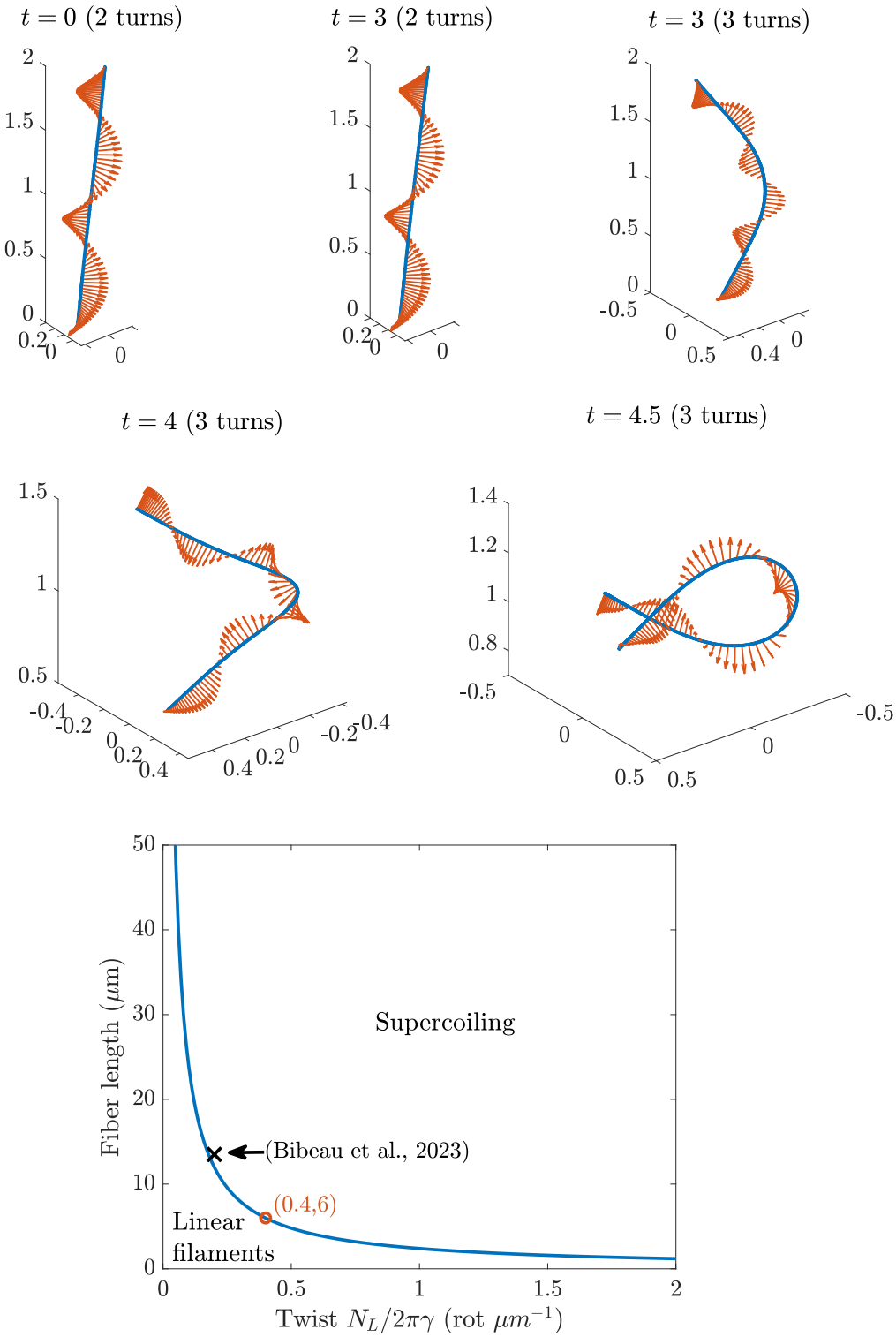

Figure S1: Supercoiled actin filaments. Top plot: behavior of perturbed filaments for 2 absolute twisted rotations (relaxing to straight) and 3 rotations (supercoiling). Bottom: Phase diagram for supercoiling as a function of the fiber length L and twist. For comparison, we plot the data from [3], where the supercoiling threshold was estimated at roughly 0.2 rotations per micron with filaments of length 7–20 μm (for small applied forces).

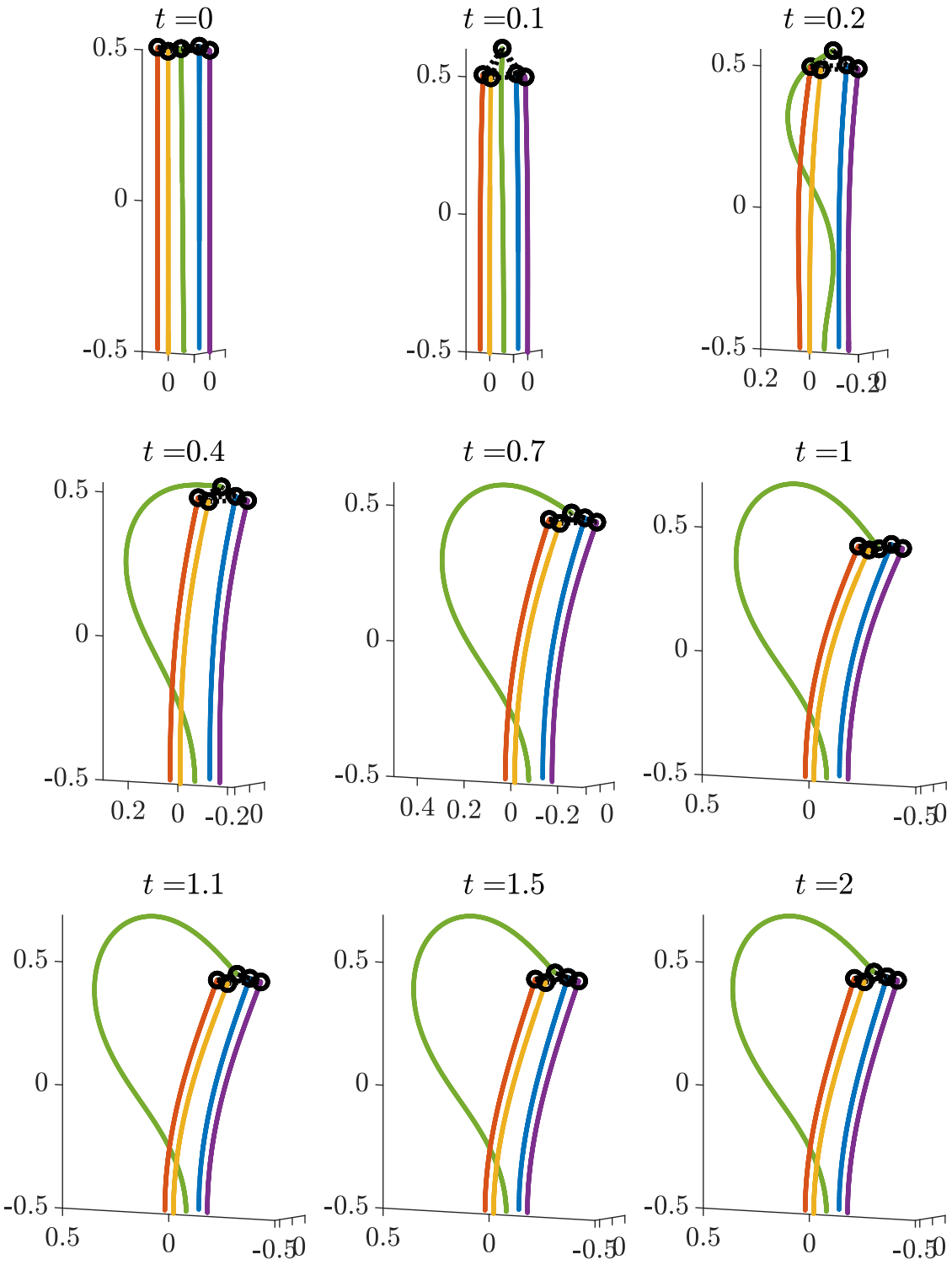

Figure S2: Initial simulation of fiber buckling with polymerization and permanent crosslinking at filament tips. The central filament polymerizes with rate 1 μm/s on $0 \leq t \leq 1$ s, after which the configuration relaxes.

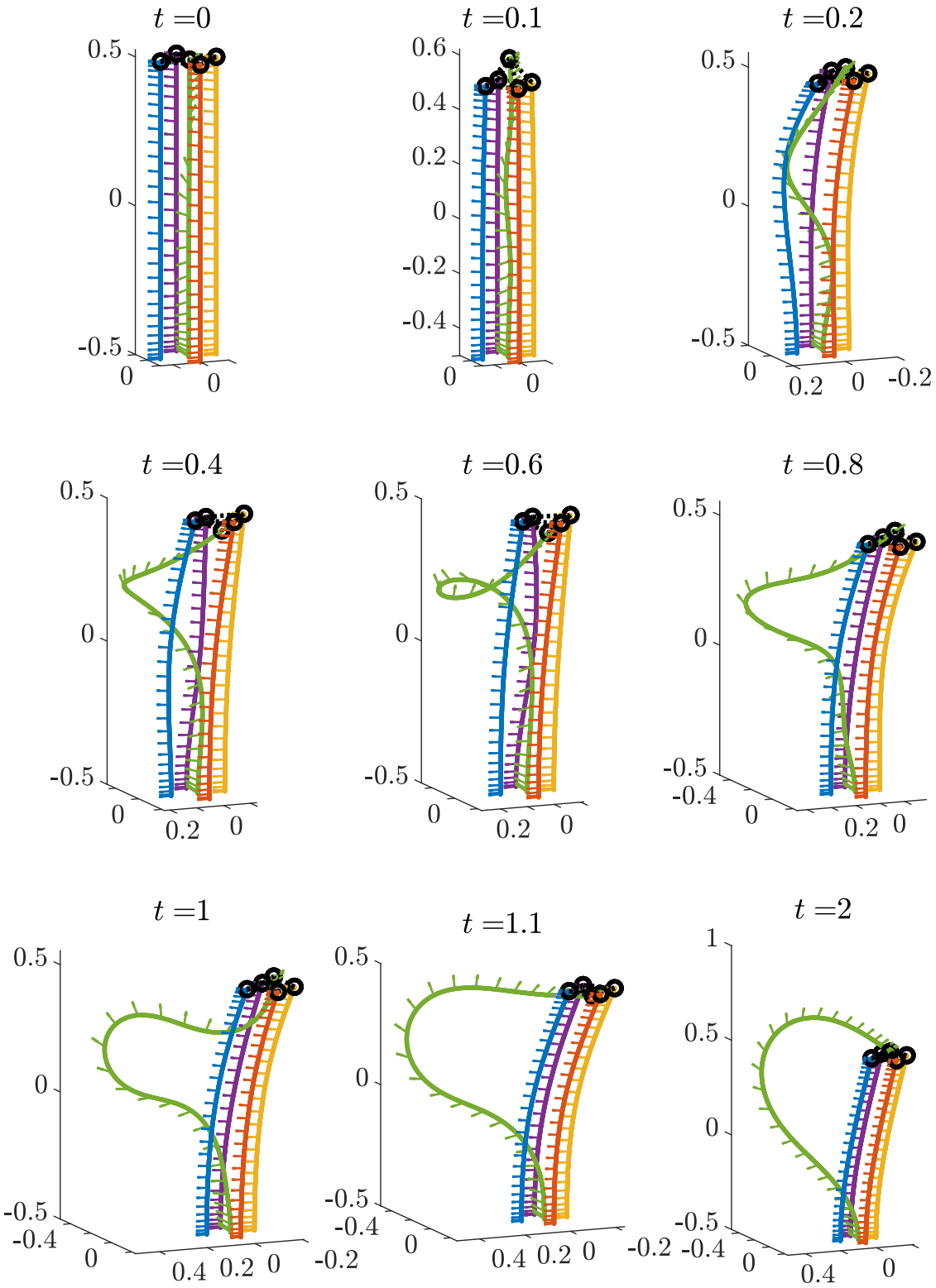

Figure S3: Buckling in a bundle due to polymerization, but with added twist along the fiber centerline using the (unrealistic) torque $N_L = 0.5$ pN·μm. Polymerization occurs only for the middle green filament, with $\dot{L} = 1$ μm/s on $0 \leq t \leq 1$ s. Arrows show the material frame vectors. Based on our linear stability analysis, we expect supercoiling when the filament length reaches ≈ 1.2 μm.

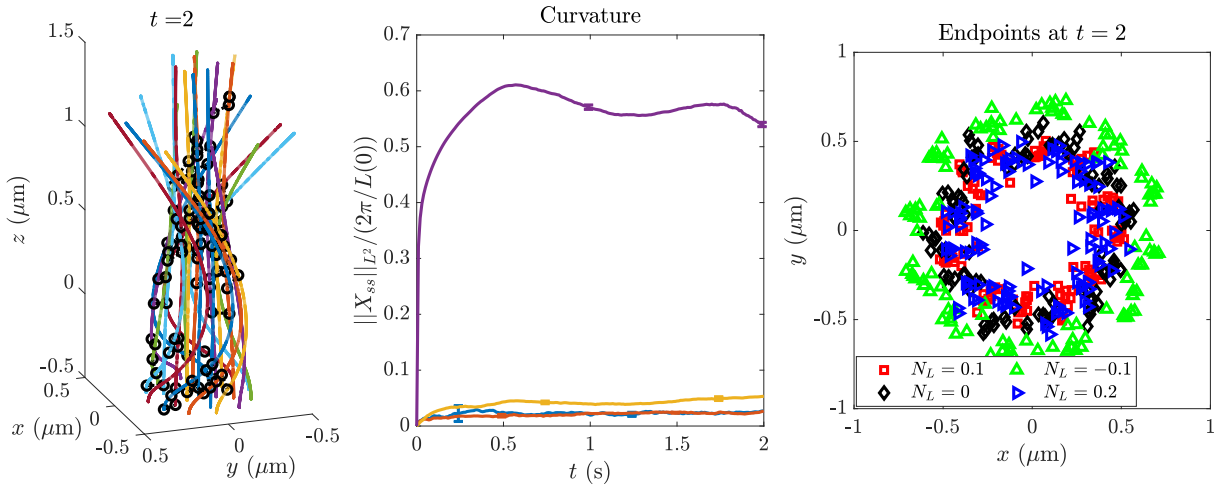

Figure S4: Effect of decreasing the range of motor activity to the lower quarter ($c_m = 1/4$, from $c_m = 1/2$) and the outer 1/8 (from 1/4) of the filopodium. Left panel: a snapshot of the filopodium at $t = 1$. Middle panel: the mean curvature on each of the four rings of filaments. Right panel: the endpoint positions at $t = 2$ with different values of the formin torque in pN·μm (similar to Fig. 5A).

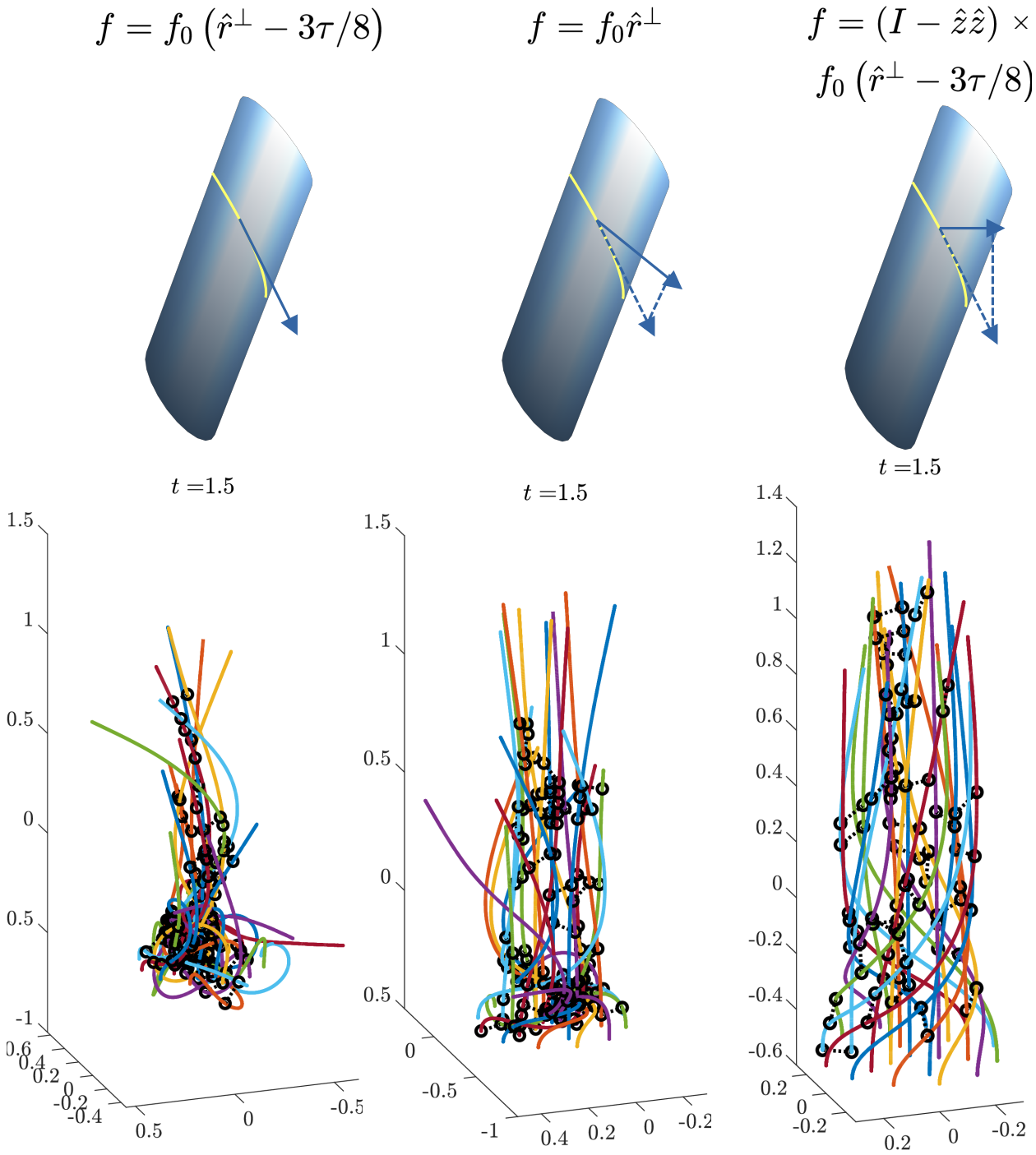

Figure S5: More detailed model of motor forces and resulting simulations. Top panel: defining the directions. The filament is shown as a blue cylinder, with the helical groove (where motors act) in yellow. The corresponding forces can be along both the normal and compressive directions (left), normal direction only (middle), or normal and compressive with downward force projected off (right). Bottom panel: simulation results (configurations at $t = 1.5$ s) considering these three different force models.

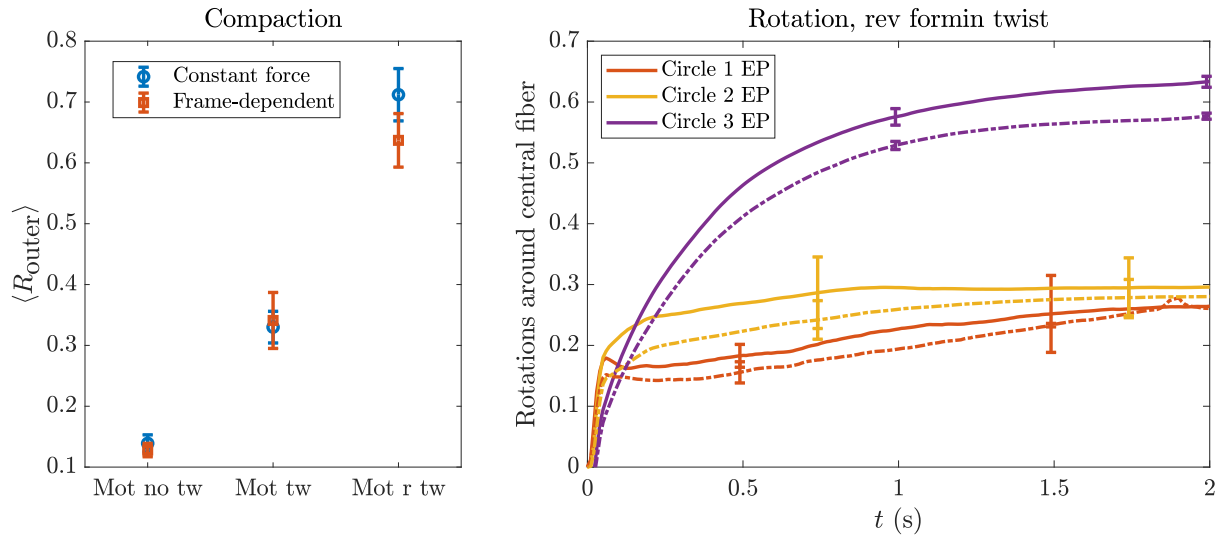

Figure S6: Statistics for simulations with fiber-orientation-dependent (or frame-dependent) forcing, as in the rightmost plot in Fig. S5. The left panel shows the compaction for simulations with CCW formin twist (left), no formin twist (middle), and CW formin twist (right), comparing our default simulations with constant forcing to the simulations with frame-dependent forcing. The rightmost plot shows the most significant difference between the two (reverse formin twist), where we see less rotation of the outer fibers when the force is frame-dependent (dotted lines) vs. when it is constant in time (solid lines).

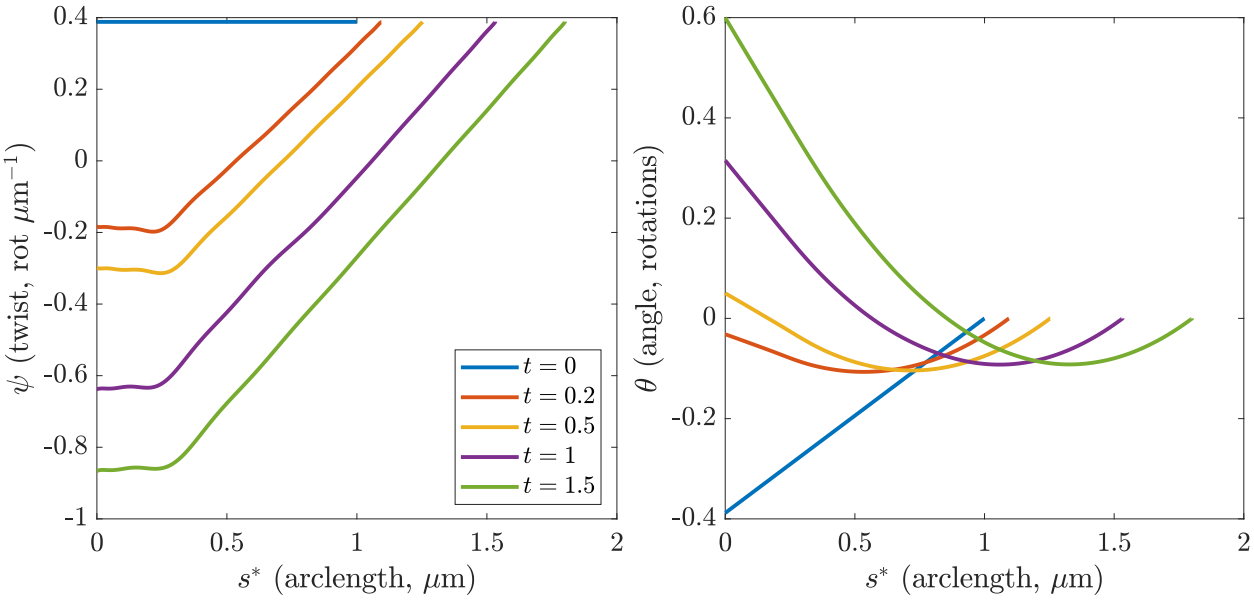

Figure S7: Twist (left, in rotations per μm) and angle of rotation (right, in rotations relative to the endpoint) over time on an outer fiber in the 22-filament bundle. This simulation has a formin torque $N_L = 0.1$ pN·μm and motor torque density $n_m = 0.2$ pN.

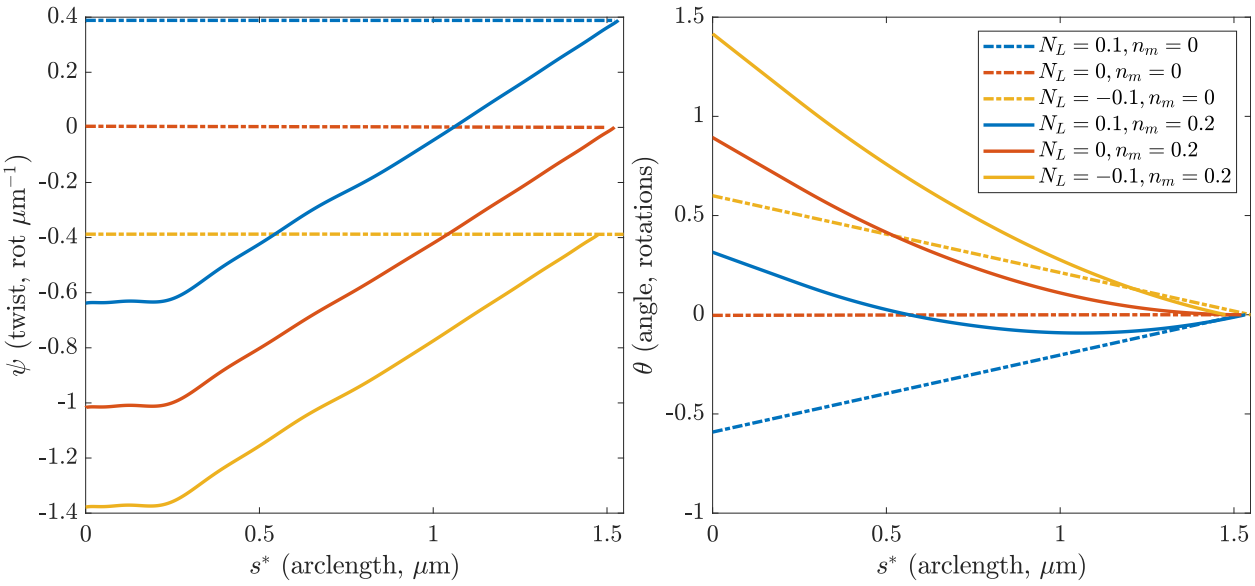

Figure S8: Twist (left, in rotations per μm) and angle of rotation (right, in rotations relative to the endpoint) on an outer fiber in the 22-filament bundle at $t = 1$ s with different parameter values for the formin torque N_L (units pN·μm) and motor torque density n_m (units pN).

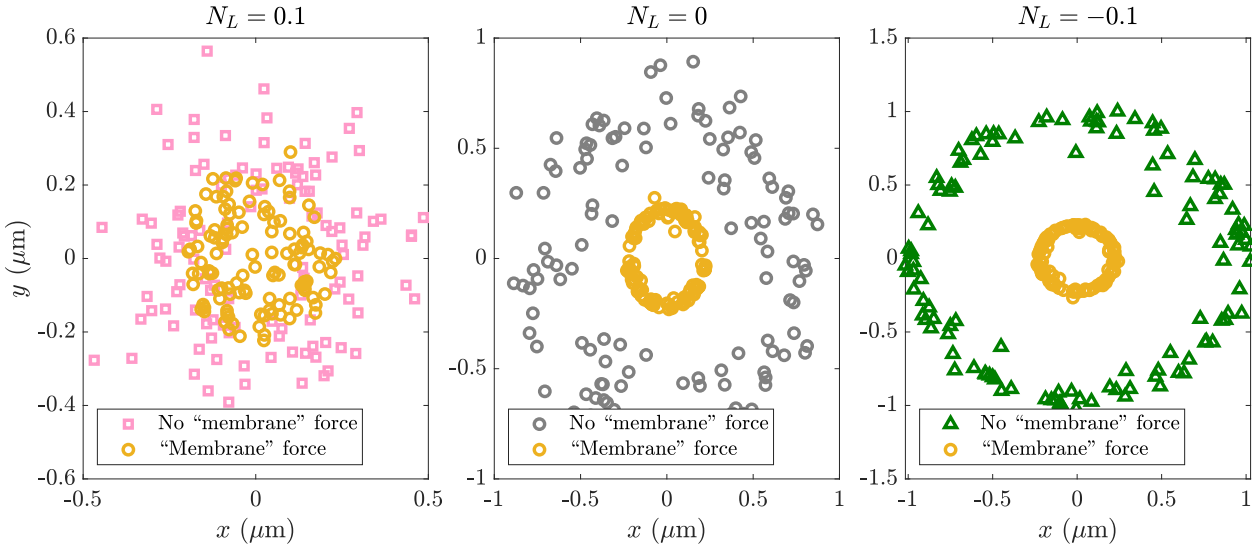

Figure S9: Endpoint position of peripheral filaments with membrane confinement. We show sets of simulations with motor force and torque and varying values of the formin twist, according to the title (units pN·μm). In each case, we project the endpoints of the peripheral filaments onto the xy plane, exactly as in Fig. 5A. In each plot, the yellow circles are simulations with confining force (intended to model the membrane), and the symbols of other colors are simulations without the confining force.

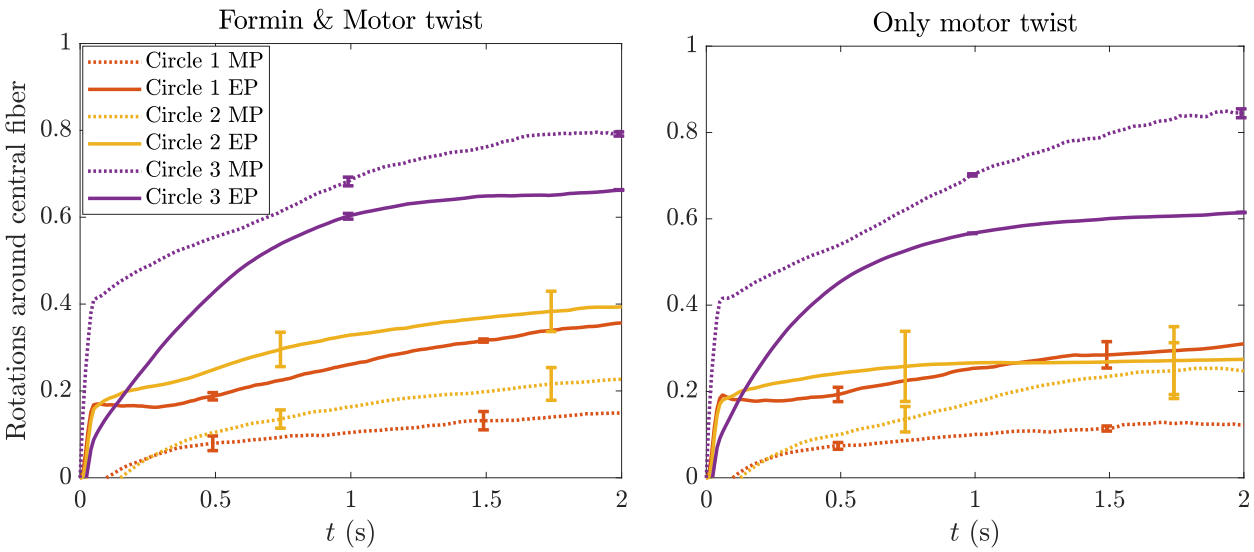

Figure S10: Number of rotations of each circle of filaments around the central filament in the 22-filament bundle. Simulations at left include motor force and torque, as well as formin torque, while simulations at right do not include formin torque. MP = midpoint, EP = endpoint.

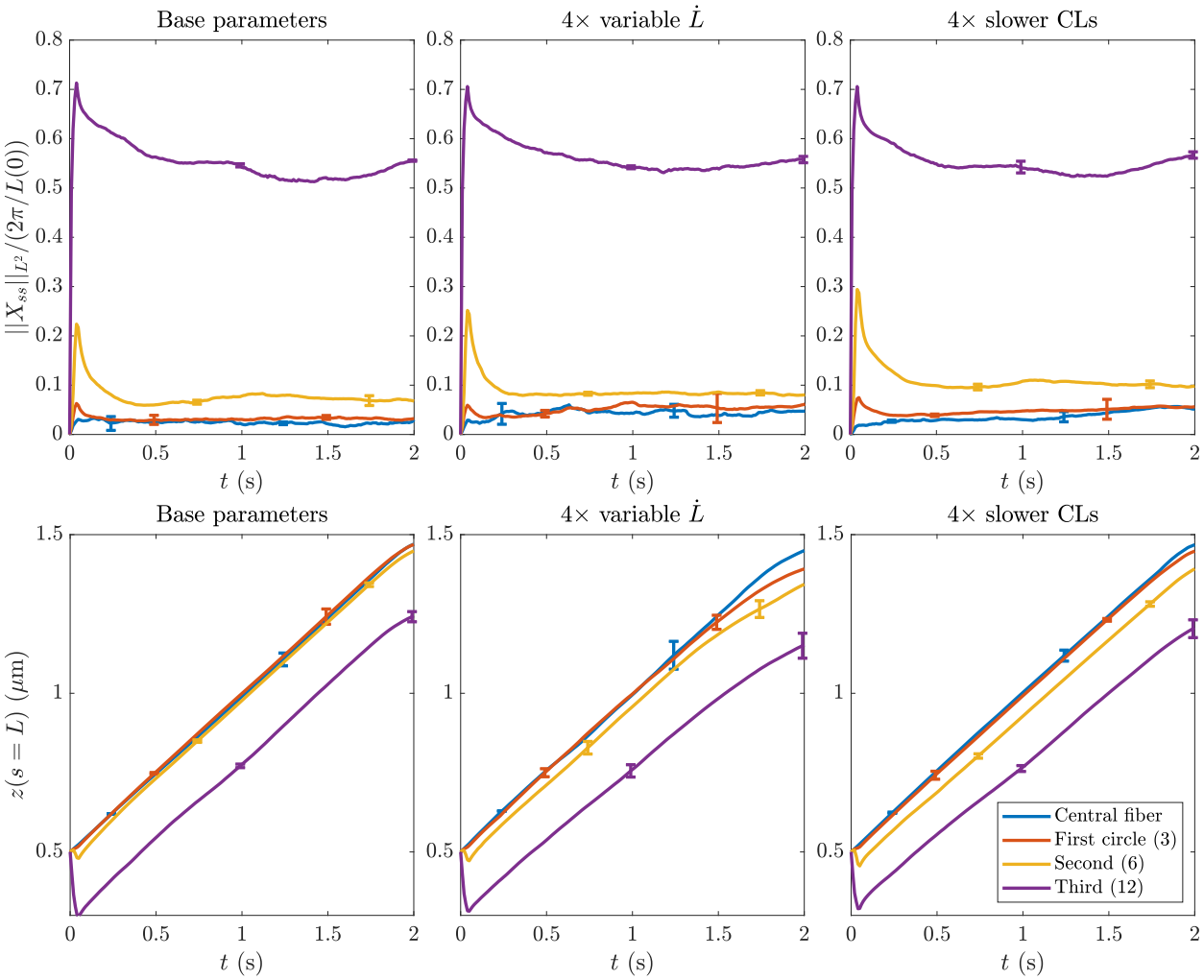

Figure S11: Bending of filaments in 22-filament bundle as a function of polymerization rate variance and cross linking rate. Top: Mean L^2 curvature of filaments, normalized by the curvature of a circle with the same circumference. Bottom: endpoint z coordinate over time. Each statistic is reported by "circle" in the bundle; blue represents the central filament, red the next circle out (3 fibers), yellow the following circle outwards (6 fibers), and purple the outermost circle (12 fibers). The outer circle has high curvature and smaller z coordinate because of motor action. From left to right, we show results for simulations with the base parameters (with motor and formin twisting), a four times larger standard deviation in the polymerization rate, and four times smaller on/off rates for the CLs.

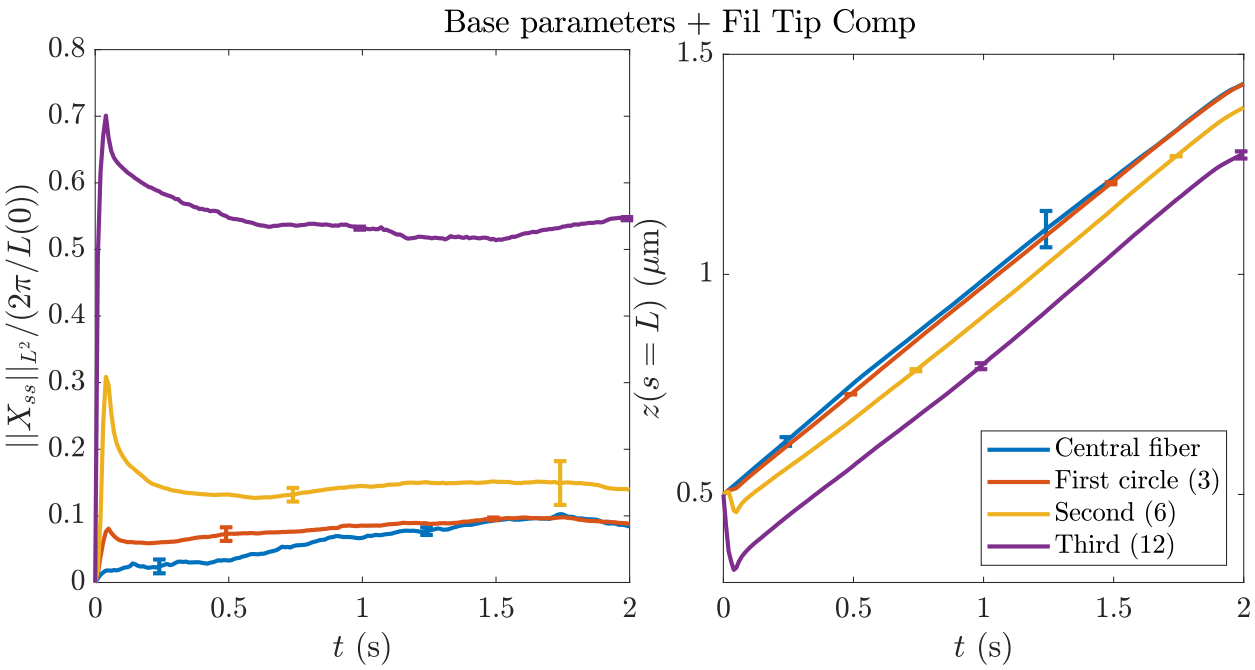

Figure S12: Bending of filaments in 22-filament bundle with the filopodial tip complex. Left: Mean L^2 curvature of filaments, normalized by the curvature of a circle with the same circumference. Right: endpoint z coordinate over time. Compared to the base parameters (left column in Fig. S11), there is more curvature and buckling with the tip complex.